





Hot Molecular Gas in the Circumnuclear Disk

Elisabeth A. C. Mills^{1,2}, Aditya Togi^{3,4} , and Michael Kaufman² ¹ Department of Astronomy, Boston University, 725 Commonwealth Avenue, Boston, MA 02215, USA; eacmills@bu.edu² Department of Physics and Astronomy, San Jose State University, 1 Washington Square, San Jose, CA 95192, USA³ Department of Physics and Astronomy, The University of Texas at San Antonio, One UTSA Circle, San Antonio, TX 78249, USA⁴ Ritter Astrophysical Research Center, University of Toledo, 2825 West Bancroft Street, MS 113, Toledo, OH 43606, USA

Received 2017 January 16; revised 2017 October 18; accepted 2017 October 18; published 2017 December 1

Abstract

We present an analysis of archival *Infrared Space Observatory* observations of H₂ for three 14'' × 20'' pointings in the central 3 pc of the Galaxy: toward the southwest region and northeast region of the Galactic center circumnuclear disk (CND), and toward the supermassive black hole Sgr A*. We detect pure rotational lines from 0–0 S(0) to S(13), as well as a number of rovibrationally excited transitions. Using the pure rotational lines, we perform both fits to a discrete temperature distribution (measuring up to three temperature components with $T = 500\text{--}600$ K, $T = 1250\text{--}1350$ K, and $T > 2600$ K) and fits to a continuous temperature distribution, assuming a power-law distribution of temperatures. We measure power-law indices of $n = 3.22$ for the northeast region and $n = 2.83$ for the southwest region. These indices are lower than those measured for other galaxies or other Galactic center clouds, indicating a larger fraction of gas at high temperatures. We also test whether extrapolating this temperature distribution can yield a reasonable estimate of the total molecular mass, as has been recently done for H₂ observations in other galaxies. Extrapolating to a cutoff temperature of 50 K in the southwest (northeast) region, we would measure 32% (140%) of the total molecular gas mass inferred from the dust emission, and 26% (125%) of the total molecular gas mass inferred from the CO emission. Ultimately, the inconsistency of the masses inferred in this way suggests that a simple application of this method cannot yield a reliable estimate of the mass of the CND.

Key words: Galaxy: center – infrared: ISM – ISM: molecules

1. Introduction

The center of our Galaxy hosts a supermassive black hole with a mass of $4 \times 10^6 M_{\odot}$ at a distance of ~ 8 kpc (Boehle et al. 2016), which is currently accreting in an extremely quiescent state, having a bolometric luminosity many orders of magnitude below the Eddington luminosity at this mass (Narayan et al. 1998; Baganoff et al. 2003). Surrounding both the black hole Sgr A* and a central nuclear star cluster (Lu et al. 2013), with an inner radius of 1–1.5 pc, is a molecular gas torus known as the circumnuclear disk (CND; e.g., Genzel et al. 1985; Güsten et al. 1987). This is the closest reservoir of molecular gas to the black hole and represents the gas available for its future feeding, activity, and associated star formation. Estimates of its mass vary, but recent studies have converged on a value of a few $\times 10^4 M_{\odot}$ (Etxaluze et al. 2011; Requena-Torres et al. 2012). The properties of this gas are much more extreme than those seen in typical molecular clouds: it has broad line widths ($\sigma \sim 10\text{--}40$ km s^{−1}) on 5'' (0.2 pc) scales indicative of strong turbulence (Christopher et al. 2005; Montero-Castaño et al. 2009), as well as high average densities of $10^5\text{--}10^6$ cm^{−3} (Requena-Torres et al. 2012; Mills et al. 2013). Some of the molecular gas is also being ionized by the nuclear star cluster (Zhao et al. 1993). Additionally, compared to the cosmic-ray ionization rate in the solar neighborhood ($\zeta \sim 3 \times 10^{-16}$ s^{−1}; Indriolo & McCall 2012) ζ is likely at least three times higher (estimates range from $>10^{-15}$ to 2×10^{-14} ; Goto et al. 2008, 2013; Harada et al. 2015). Altogether, it is perhaps the most extreme environment in our Galaxy for forming stars.

Whether or not the CND is currently forming stars is controversial. Measurements of density indicate that the broad line widths measured by Christopher et al. (2005) and

Montero-Castaño et al. (2009) are highly supervirial, and the clumps are therefore not self-gravitating (Smith & Wardle 2014). Despite this, there have been suggestions of star formation based on several indicators, including shock-excited methanol masers and candidate outflows traced by SiO (5–4) (Yusef-Zadeh et al. 2015), as well as compact, highly excited SiO emission interior to the CND (Yusef-Zadeh et al. 2013b). However, the bulk of these have other plausible explanations: methanol masers can be excited in strong shocks and are ubiquitous throughout the Galactic center in the absence of other signs of star formation (Yusef-Zadeh et al. 2013a; Mills et al. 2015), and in fact many of the masers highlighted by Yusef-Zadeh et al. (2015) are at velocities not associated with CND gas. Line widths in the CND, as noted above, are generally broad with complex profiles that can be attributed to extreme turbulence in this source. Finally, in the vicinity of the strong radiation field from a nuclear star cluster, the detection of highly excited SiO may indicate radiative excitation (Godard & Cernicharo 2013) rather than denser gas that could be associated with a protostar. At present, then, conclusive evidence for active star formation in the CND is lacking, and this structure appears, like many other Galactic center clouds (e.g., Longmore et al. 2013), to be relatively quiescent.

Although observations motivated by constraining star formation have led to estimates of the gas density, we are still lacking the full picture of the physical conditions that dominate in this region. In particular, new observations have failed to yield improved estimates of the gas temperature in this region. The temperature is unconstrained in the analysis of Mills et al. (2013) using HCN and HCO⁺ over a range from 50 to 300 K. While Bradford et al. (2005) report a temperature of $\sim 200\text{--}300$ K using CO, they acknowledge that there are no

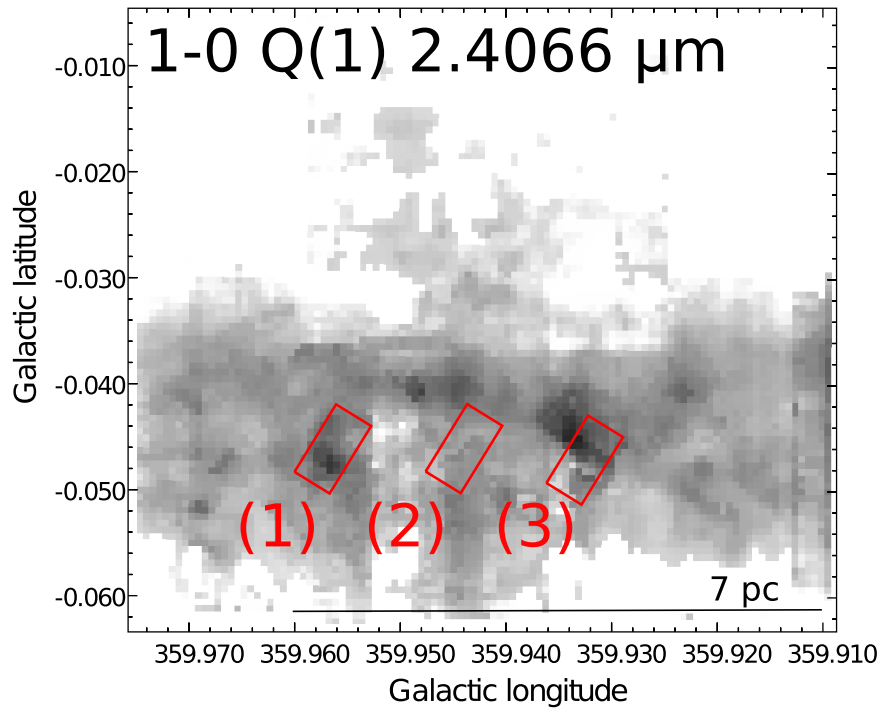


Figure 1. Locations of the *ISO*/SWS apertures for the observed H_2 spectra, superposed on a map of the 1–0 Q(1) line of H_2 taken with the near-infrared long-slit spectrograph ISAAC on the Very Large Telescope using drift scans (Feldmeier et al. 2014). The ISAAC data have a resolution (pixel size) of $2''.22$. The *ISO*/SWS aperture size shown here is $14'' \times 20''$. Position (1) corresponds to the northeast region of the CND, position (2) corresponds to Sgr A*, and position (3) corresponds to the southwest region of the CND.

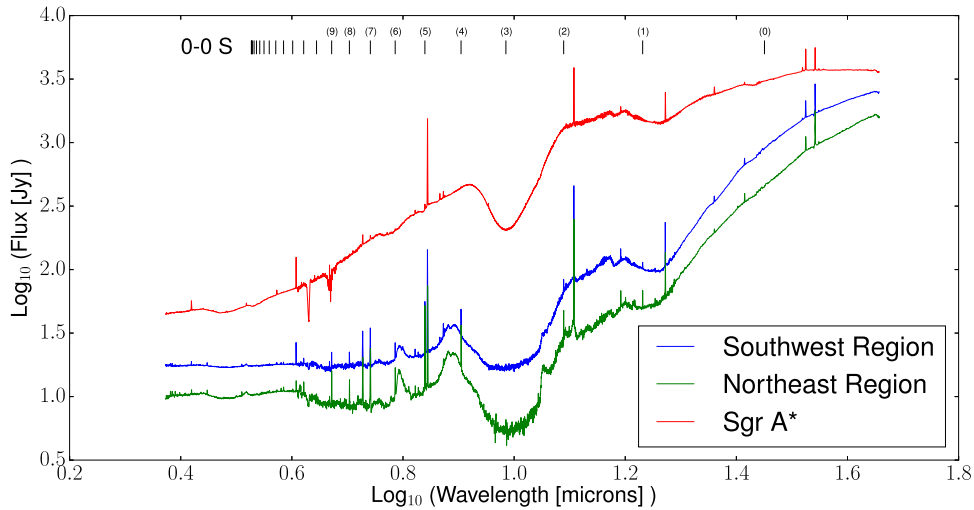


Figure 2. SWS spectra for the three positions observed with *ISO* toward the central parsecs of the Galaxy: Sgr A*, the northeast region of the CND, and the southwest region of the CND. Wavelengths corresponding to the 0–0 S pure rotational lines are indicated. The aperture size changes at 12, 27.5, and 29 μm ; however, the spectra have been scaled so that the continuum level is consistent across these changes.

stringent upper limits on this value. This is consistent with earlier observations of Lugten et al. (1987), as well as observations of a larger number of CO transitions by Requena-Torres et al. (2012) that constrain the temperature only to be $\gtrsim 150$ K, over a range of considered temperatures that extends up to 600 K. While Hermstein & Ho (2002) detect the highly excited NH_3 (6, 6) line ($E_{\text{upper}} \sim 400$ K), they do not calculate a gas temperature from their observations. In comparison, many more observational constraints on the dust temperature exist: dust temperatures as warm as 90 K have been measured, though these are only suggested to apply to a

small fraction ($< 10\%$) of the CND mass (Etxaluz et al. 2011; Lau et al. 2013). However, this may not give any constraint on the dust temperature, as the gas and dust temperatures are observed to be decoupled in Galactic center clouds (e.g., Ginsburg et al. 2016), and the gas densities present may not be high enough that the gas and dust would be expected to be thermalized here, given the high cosmic-ray ionization rate (Clark et al. 2013; Goto et al. 2013).

Inside the central cavity of the CND, the gas is predominately atomic (Jackson et al. 1993), with an estimated mass of $300 M_{\odot}$, and its temperature is also not constrained. However,

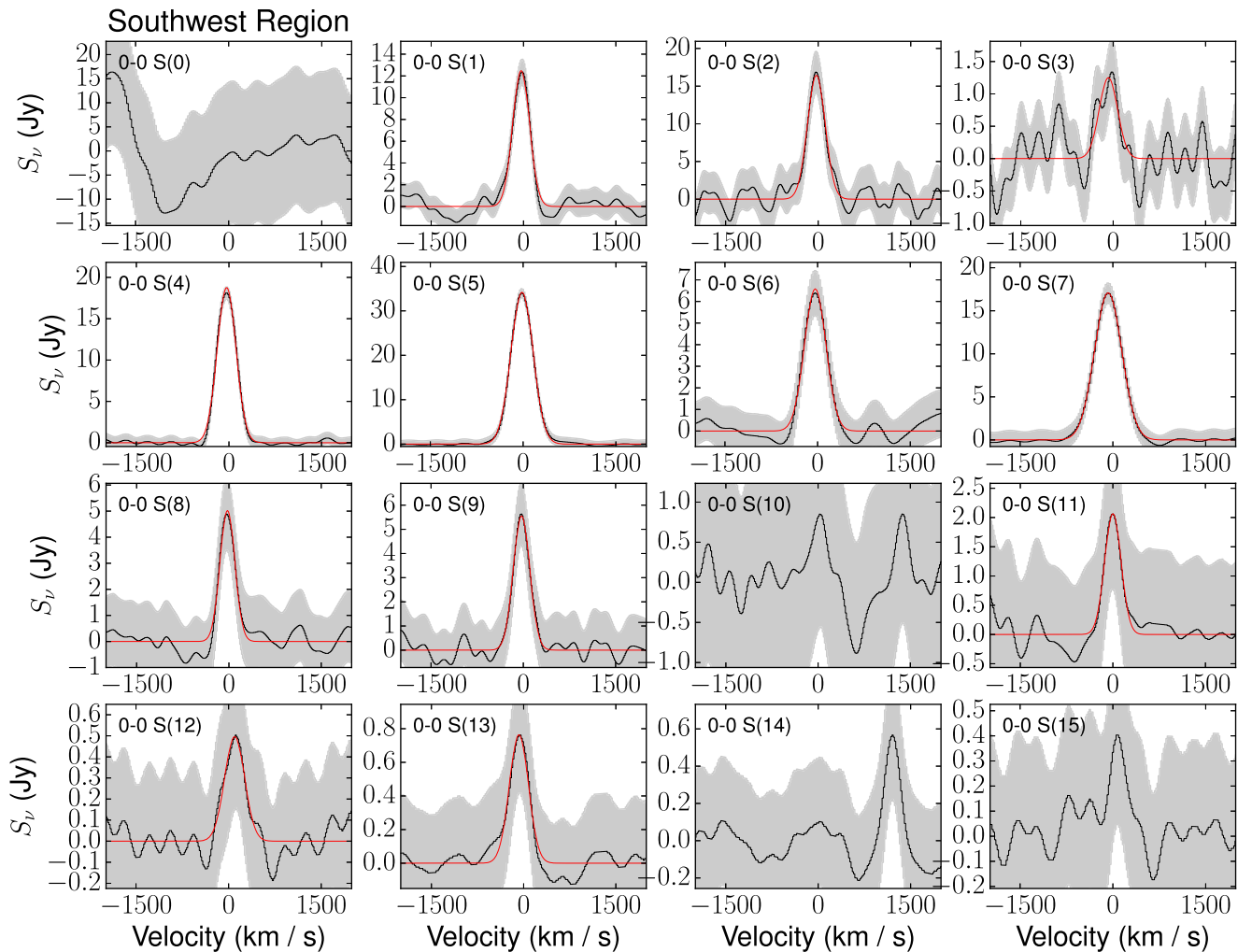


Figure 3. Spectra of the pure rotational lines of H_2 from 0–0 S(0) to S(15) toward the southwest region, northeast region, and Sgr A*. The amplitude uncertainty at each wavelength is shown in gray shading. Gaussian fits to all of the significantly detected lines are overlotted in red.

there is also an ionized component (the “minispiral”; Ekers et al. 1983; Lo & Claussen 1983) with about 10% of the mass of the atomic component, for which the temperature of the intermixed dust is measured to be as high as 220 K (Cotera et al. 1999). There is also suggested to be a hot molecular component, as highly excited CO is detected toward Sgr A* with *Herschel* (Goicoechea et al. 2013) that is consistent with temperatures of ~ 1300 K. Resolved observations of the inner edge and cavity of the CNB in rovibrational lines of H_2 have been made by Ciurlo et al. (2016) and indicate temperatures up to a few thousand kelvin, with the total mass of gas at these temperatures being $< 10^{-2} M_{\odot}$. However, much of the cavity gas also shows strong deviations from thermal equilibrium.

Accurate gas temperature measurements in the central parsecs are critical for advancing our understanding of the CNB on several fronts. First, improved constraints on the temperature are needed for better constraints on the density. Without strong constraints on the gas temperature, the degeneracy between high-temperature/low-density and low-temperature/high-density solutions to radiative transfer models leads to orders-of-magnitude uncertainty in density measurements (e.g., Requena-Torres et al. 2012; Mills et al. 2013; Smith & Wardle 2014). More precise measurements of the gas density structure are needed in order to better assess the evolution, longevity, and

star-forming potential of this structure. Improved constraints on the temperature are also needed to determine the dominant heating mechanism for the dense molecular gas in the CNB. Cosmic rays (Goto et al. 2008; Harada et al. 2015), UV radiation (Lau et al. 2013; Ciurlo et al. 2016), X-rays (Goto et al. 2013), and turbulent dissipation (Lugten et al. 1987) have all been suggested to contribute to the heating in this environment. Isolating the dominant heating source is relevant for determining the extent to which the CNB gas may be taken to be an analog for gas in the centers of more extreme galaxies like ULIRGs, nuclear starbursts, or even active galactic nuclei.

In clouds in the central 300 pc of the Galactic center, most gas temperature measurements have been made with NH_3 (Güsten et al. 1985; Hüttemeister et al. 1993; Mills & Morris 2013), other symmetric tops like CH_3CN and CH_3CCH (Güsten et al. 1985), CO (Martin et al. 2004), and more recently H_2CO (Ao et al. 2013; Ginsburg et al. 2016). However, in the CNB these tracers have not yielded well-defined temperatures. H_2CO is extremely weak in the CNB, likely due to photodissociation (Martín et al. 2012), and the same is true of CH_3CN and CH_3CCH (D. Riquelme 2017, private communication). As already noted, analyses of CO and NH_3 have also failed to yield well-defined constraints on temperature (Lugten et al. 1987; Herrnstein & Ho 2002;

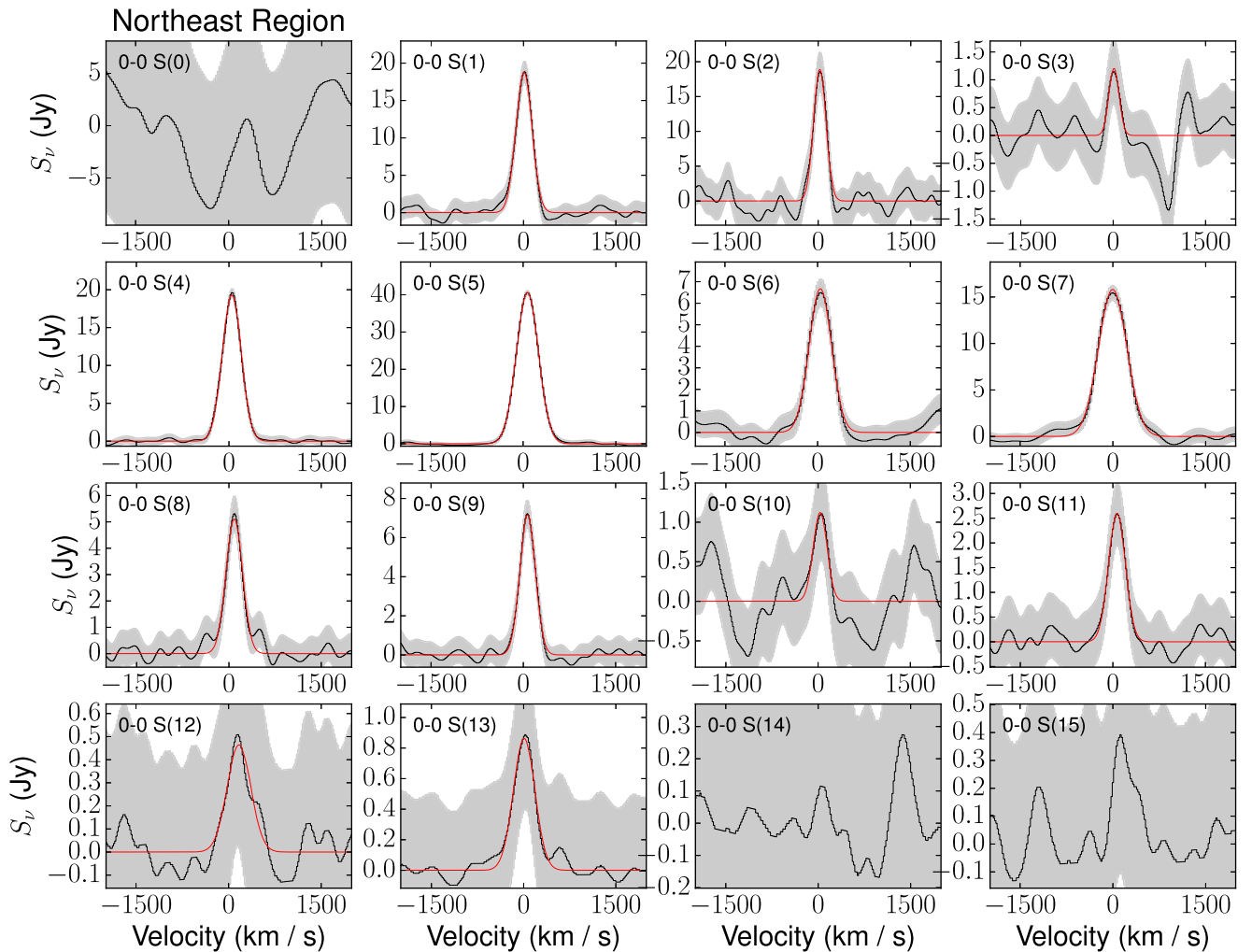


Figure 3. (Continued.)

Requena-Torres et al. 2012). In this paper, we undertake an alternative approach by directly measuring the temperature of the gas using H_2 . Typically, due to a combination of the lack of a permanent dipole moment of H_2 and the relatively high energy of the lowest rotational transition (510 K), H_2 is not a detectable tracer of the cool molecular ISM, and one must rely on the previously listed indirect tracers of gas temperature. However, clouds in the Galactic center are much warmer, and so these lines can be detected in a significant fraction of the gas. As an example, Rodríguez-Fernández et al. (2001) detect pure rotational lines of H_2 in a sample of 16 Galactic center clouds and measure gas with temperatures from 150 to 600 K that composes 30% of the total H_2 column.

In this paper, we undertake an analysis of archival *Infrared Space Observatory* (*ISO*) spectra of pure rotational and rovibrational lines of H_2 in three positions toward the CND and central parsec. There are a number of prior observations of rovibrational lines in the near-infrared (Yusef-Zadeh et al. 2001; Lee et al. 2008; Feldmeier et al. 2014; Ciurlo et al. 2016); however, to our knowledge this is the first analysis of the pure rotational lines in this source. We present a temperature analysis of these lines that includes both a fit to a discrete number of temperature components and a power-law analysis assuming a continuous distribution of temperatures. We then discuss the fraction of warm H_2 that is detected in the

CND, the implications of this temperature distribution for identifying a heating source, and the uniqueness of the CND compared to other sources in which H_2 temperatures have been measured.

2. Data

The data used in the analysis in this paper were obtained from the NASA/IPAC Infrared Science Archive. We analyzed spectra from three positions observed with *ISO* (Kessler et al. 1996) toward the central 2 pc of the Milky Way. All observations were made in 1996 May using the Short Wavelength Spectrograph (SWS; de Graauw et al. 1996) in low-resolution, full-grating scan mode. Spectra of the central pointing toward the black hole Sgr A* (TDT no. 09401801, R.A. = $17^{\text{h}}45^{\text{m}}39^{\text{s}}.97$, decl. = $-29^{\circ}00'28''.7$) were published in Lutz et al. (1996); however, the H_2 lines were not analyzed. The other two pointings, toward the northeast region (TDT no. 09401504, R.A. = $17^{\text{h}}45^{\text{m}}41^{\text{s}}.76$, decl. = $-28^{\circ}59'50''.7$) and the southwest region (TDT no. 09401905, R.A. = $17^{\text{h}}45^{\text{m}}38^{\text{s}}.58$, decl. = $-29^{\circ}01'05''.8$), have not been published.

The spectra were obtained with an aperture of $14'' \times 20''$ for wavelengths of 2.38–12.0 μm , $14'' \times 27''$ for wavelengths of 12.0–27.5 μm , and $20'' \times 27''$ for wavelengths of 27.5–29.0 μm . Only the 0–0 S(0) H_2 line at a wavelength of 28.221 μm is

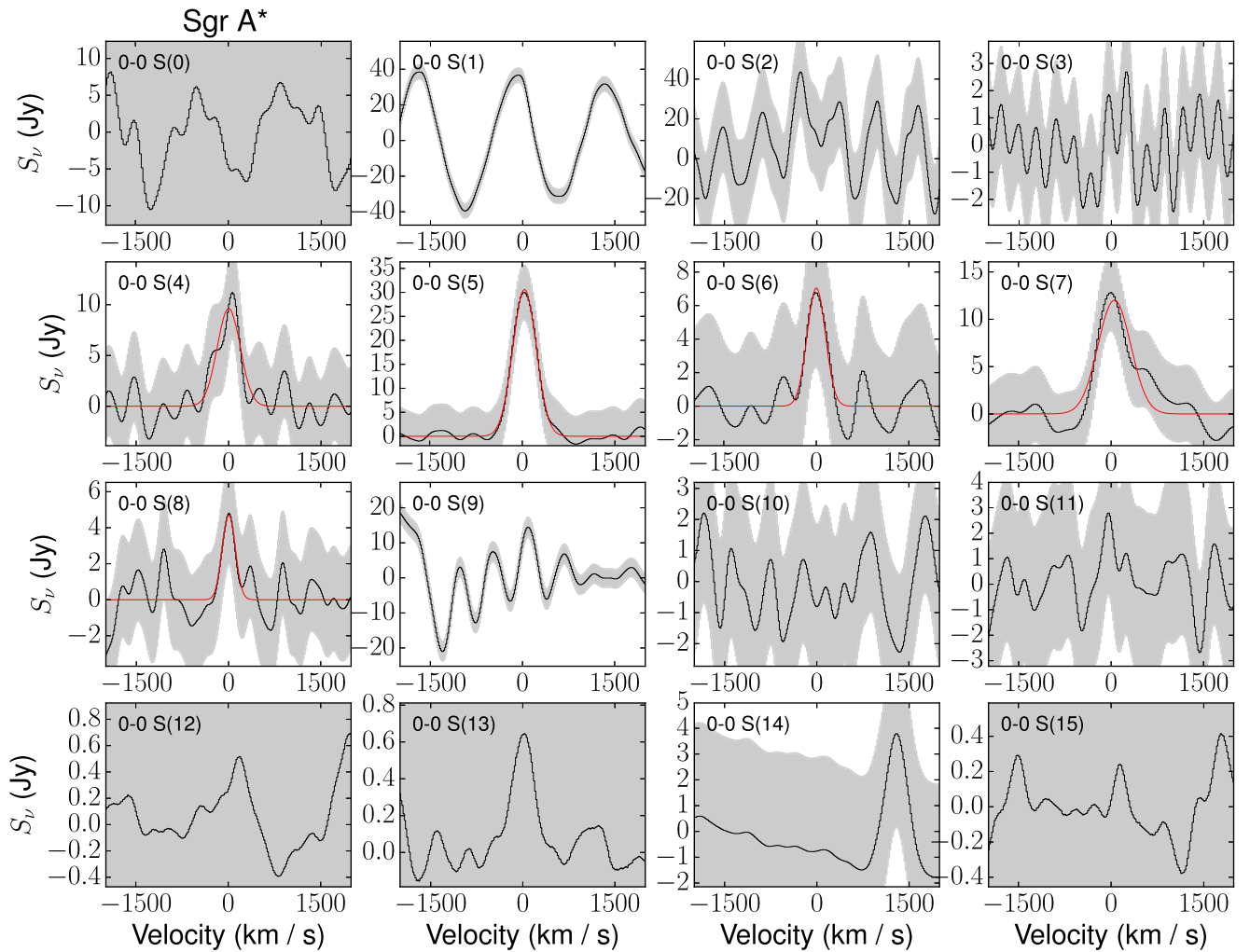


Figure 3. (Continued.)

observed with an aperture of $20'' \times 27''$. The 0–0 S(1) and S(2) lines are observed with an aperture of $14'' \times 27''$, and the remainder of the lines are observed with a consistent aperture of $14'' \times 20''$. However, the SWS spectra we use are highly processed data products that have had their continuum level normalized to a consistent value (Sloan et al. 2003). Based on mapped observations of the 1–0 Q(1) line (Feldmeier et al. 2014), we assume that the H_2 emission can be taken to fill the aperture with a filling fraction of 1 for this range of aperture sizes, and so in subsequent calculations we take the effective aperture size to be $14'' \times 20''$ and apply no additional correction for variations in the aperture size between lines. For all aperture sizes, the long axis of the slit is oriented with a position angle of -1.4° in an ecliptic coordinate frame. The position of these pointings is shown in Figure 1, superposed on the map of the 1–0 Q(1) line from Feldmeier et al. (2014).

The full spectra toward each position from 2.5 to $40 \mu\text{m}$ are shown in Figure 2. Integration times for these observations were 6528 s, resulting in per-channel noise levels of ~ 0.5 –1 Jy for all lines except the 0–0 S(0) line, which has a noise of ~ 10 Jy. Additional baseline fluctuations with amplitudes 0.5–1 Jy are present in the spectra, which can become as high as 5–40 Jy toward Sgr A*. The channel width of the observations is $\sim 15 \text{ km s}^{-1}$; however, the actual instrumental spectral resolution is $R \sim 1000$ –3000, or 100–300 km s^{-1} .

We fit a first-order polynomial to the continuum in the $\pm 2000 \text{ km s}^{-1}$ surrounding the line. The continuum levels range from 10 to 3000 Jy, and the shapes are generally well fit by this approach. For the S(0) line, the continuum is larger, with a steeper slope and greater variation. For this line, we fit a first-order polynomial to a more limited range. The baseline-subtracted spectra of the 0–0 S, 1–0 Q, and 1–0 O lines are shown in Figures 3–5.

3. Results and Analysis

We detect multiple pure rotational and rovibrational lines of H_2 toward all three positions. The strongest H_2 emission is detected from the north, with slightly weaker emission in the southwest and toward Sgr A*. Toward the southwest region we detect 12 pure rotational lines, up to 0–0 S(13), and 7 rovibrational lines, up to 1–0 Q(5) and 1–0 O(6). Toward the northeast region we detect 13 pure rotational lines, up to 0–0 S(13), and 10 rovibrational lines, up to 1–0 Q(7) and 1–0 O(6). This is half the number of H_2 pure rotational and rovibrational lines that have been detected by SWS toward the Orion KL outflow (56; Rosenthal et al. 2000). Toward Sgr A* we detect only five pure rotational lines from S(4) to S(8), and we only detect two rovibrational lines: O(4) and O(5). The continuum is significantly stronger toward Sgr A*, and the baseline structures are more complicated, hindering the detection of a similarly

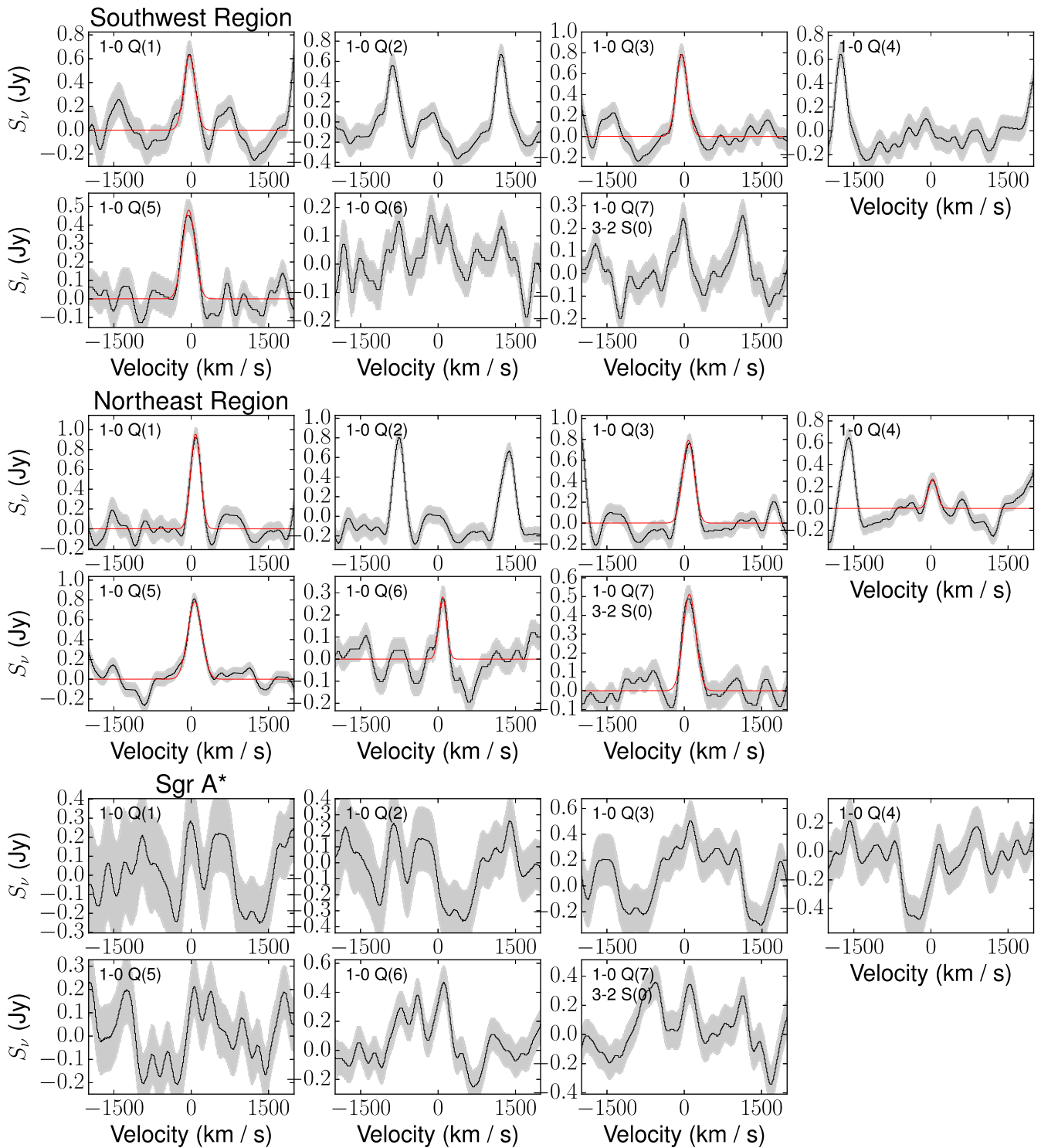


Figure 4. Spectra of the 1–0 Q(1) through Q(7) lines toward the southwest region, northeast region, and Sgr A*. The amplitude uncertainty at each wavelength is shown in gray shading. Gaussian fits to all of the significantly detected lines are overplotted in red.

large number of lines in this source. Typical baseline uncertainties are 0.3 Jy for N and S and 0.7 Jy for Sgr A*.

We fit Gaussian profiles to all of the detected lines (shown in Figures 3–5) and report the line parameters for each source in Tables 1–3. Typical measured line widths are $\sim 140 \pm 40$ km s⁻¹, so considering that the spectral resolution of these SWS observations ranges from 100 to 300 km s⁻¹ (Valentijn et al. 1996), the lines are likely not resolved, and their shape is dominated by the instrumental profile. Additionally, the central

velocities show variation within each source, on the order of 30–40 km s⁻¹, which can be attributed to the uncertainty in the wavelength calibration of these observations, which has been measured to range from 25 to 60 km s⁻¹ (Valentijn et al. 1996). We measure a mean central velocity of -34 ± 38 km s⁻¹ toward the southwest region, 57 ± 38 km s⁻¹ toward the northeast region, and 28 ± 25 km s⁻¹ toward Sgr A*.

There are several lines for which it appears that there is a contaminating line at nearly the same wavelength. The 1–0

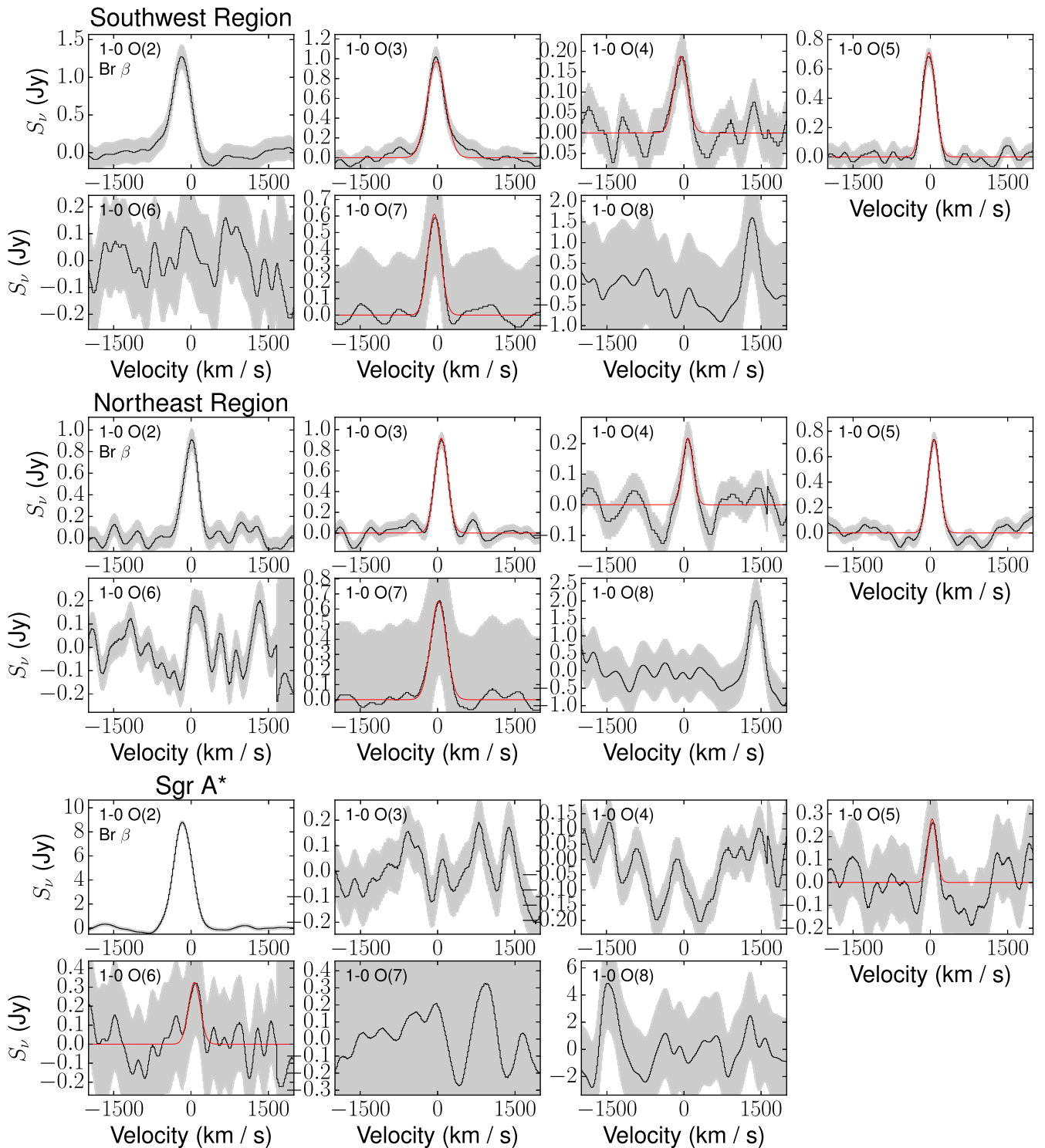


Figure 5. Spectra of the 1–0 O(2) through O(8) lines toward the southwest region, northeast region, and Sgr A*. The amplitude uncertainty at each wavelength is shown in gray shading. Gaussian fits to all of the significantly detected lines are overplotted in red.

O(2) line at $2.62688 \mu\text{m}$ shows two signatures indicative of contamination with a species tracing the ionized gas: it is anomalously strong compared to other nearby H_2 lines, and the emission toward Sgr A* is stronger than the emission toward the two pointings in the CNB, which is not observed in other H_2 lines. In addition, the 1–0 O(2) line appears offset from the velocity inferred from the H_2 lines. Based on the strength and velocity of the feature near the 1–0 O(2) line, we identify this as the Brackett β line at $2.62587 \mu\text{m}$ at an offset velocity of

114 km s^{-1} . Contamination with this line is also noted in SWS observations of NGC 1068 by Lutz et al. (2000). In addition, the wavelengths of the 1–0 Q(7) line at $2.5001 \mu\text{m}$ and the 3–2 S(0) line at $2.5014 \mu\text{m}$ are nearly overlapping (having an offset velocity of 183 km s^{-1}). If we assume that the feature detected at this wavelength is 3–2 S(0), then the measured velocity is significantly offset from that measured for the other H_2 lines. We thus infer that the emission here is dominated by the 1–0 Q(7) line, and we do not report a detection of the 3–2 S(0) line.

Table 1
Fitted Line Parameters for Southwest Region

λ	E_{upper}	g_J	Flux	Central ^a Velocity	Velocity ^b FWHM	Integrated Flux ^c	$N(\text{H}_2)^c$	A_λ	
(μm)	(K)		(Jy)	(km s^{-1})	(km s^{-1})	(Jy km s^{-1})	(cm^{-2})		
0–0 S(0)	28.221	510	5	<43.8	<4659	$<1.5 \times 10^{21}$	0.97
0–0 S(1)	17.035	1015	21	12.5 ± 0.4	-38 ± 4	137 ± 4	1825 ± 98	$3.69 \pm 0.20 \times 10^{19}$	1.57
0–0 S(2)	12.279	1682	9	16.4 ± 0.7	-30 ± 7	143 ± 7	2518 ± 224	$8.77 \pm 0.78 \times 10^{18}$	1.31
0–0 S(3)	9.665	2504	33	1.3 ± 0.2	-77 ± 20	149 ± 20	198 ± 45	$1.94 \pm 0.45 \times 10^{17}$	5.26
0–0 S(4)	8.026	3474	13	18.8 ± 0.2	-37 ± 2	152 ± 2	3040 ± 69	$1.11 \pm 0.03 \times 10^{18}$	1.00
0–0 S(5)	6.909	4586	45	34.2 ± 0.3	-17 ± 1	178 ± 1	6491 ± 110	$1.06 \pm 0.02 \times 10^{18}$	0.88
0–0 S(6)	6.109	5829	17	6.6 ± 0.4	-38 ± 11	174 ± 11	1220 ± 120	$1.03 \pm 0.10 \times 10^{17}$	1.07
0–0 S(7)	5.511	7197	57	17.1 ± 0.4	-76 ± 5	220 ± 5	4020 ± 162	$1.93 \pm 0.08 \times 10^{17}$	0.93
0–0 S(8)	5.053	8677	21	5.0 ± 0.4	-23 ± 12	121 ± 12	647 ± 105	$1.92 \pm 0.31 \times 10^{16}$	0.98
0–0 S(9)	4.695	10263	69	5.6 ± 0.4	-28 ± 11	134 ± 11	792 ± 107	$1.55 \pm 0.21 \times 10^{16}$	1.26
0–0 S(10)	4.410	11940	25	<4.2	<449	$<6.1 \times 10^{15}$	1.05
0–0 S(11)	4.181	13703	81	2.1 ± 0.4	0 ± 32	133 ± 32	293 ± 111	$2.92 \pm 1.12 \times 10^{15}$	1.11
0–0 S(12)	3.995	15549	29	0.5 ± 0.1	98 ± 40	161 ± 40	85 ± 34	$6.45 \pm 2.62 \times 10^{14}$	1.13
0–0 S(13)	3.846	17458	93	0.8 ± 0.1	-76 ± 26	155 ± 26	126 ± 34	$7.52 \pm 2.03 \times 10^{14}$	1.19
0–0 S(14)	3.724	19402	33	<1.0	<110	$<5.3 \times 10^{14}$	1.27
0–0 S(15)	3.625	21400	105	<1.1	<112	$<4.5 \times 10^{14}$	1.36
1–0 Q(1)	2.407	6149	9	0.6 ± 0.0	-31 ± 7	109 ± 7	73 ± 8	$1.64 \pm 1.64 \times 10^{15}$	2.21
1–0 Q(2)	2.413	6471	5	<0.3	<50	$<1.6 \times 10^{15}$	2.20
1–0 Q(3)	2.424	6956	21	0.8 ± 0.0	-51 ± 5	108 ± 5	90 ± 7	$3.14 \pm 3.14 \times 10^{15}$	2.18
1–0 Q(4)	2.438	7584	9	<0.3	<47	$<1.7 \times 10^{15}$	2.16
1–0 Q(5)	2.455	8365	33	0.5 ± 0.0	-49 ± 8	122 ± 8	62 ± 6	$2.36 \pm 2.36 \times 10^{15}$	2.13
1–0 Q(6)	2.476	9286	13	<0.2	<32	$<1.3 \times 10^{15}$	2.09
1–0 Q(7)	2.500	10341	45	<0.2	<32	$<1.3 \times 10^{15}$	2.05
1–0 O(2)	2.627	5987	1	<0	<74	$<8.4 \times 10^{14}$	1.85
1–0 O(3)	2.803	6149	9	1.0 ± 0.0	-24 ± 6	175 ± 6	182 ± 10	$4.14 \pm 0.24 \times 10^{15}$	1.89
1–0 O(4)	3.004	6471	5	0.2 ± 0.0	-60 ± 14	129 ± 14	25 ± 4	$8.61 \pm 1.57 \times 10^{14}$	2.28
1–0 O(5)	3.235	6956	21	0.7 ± 0.0	-27 ± 3	123 ± 3	94 ± 4	$4.33 \pm 0.21 \times 10^{15}$	1.85
1–0 O(6)	3.501	7584	9	<1	<89	$<5.8 \times 10^{15}$	1.58
1–0 O(7)	3.808	8365	33	0.6 ± 0.1	-62 ± 29	126 ± 29	82 ± 30	$7.50 \pm 2.73 \times 10^{15}$	1.20
1–0 O(8)	4.162	9286	13	<4	<630	$<8.2 \times 10^{16}$	1.08

Notes.

^a Uncertainty in the wavelength calibration of *ISO* observations ranges from 25 to 60 km s^{-1} (Valentijn et al. 1996).

^b The spectral resolution of SWS observations ranges from 100 to 300 km s^{-1} (Valentijn et al. 1996).

^c Values are not corrected for extinction.

There are also several lines for which there are features at nearby wavelengths that appear as emission at offset velocities (e.g., in the 1–0 O(8) and 1–0 Q(2) lines and the 2–1 O(6) line) that are likely due to other species.

From the Gaussian fits to the flux of each line, we can calculate a column density for each level using the relation

$$N(v, J) = \frac{4\pi\lambda I_{\text{obs}}(v, J - v', J')}{hc A_{ul}(v, J - v', J')} e^{A(\lambda)/1.086}, \quad (1)$$

where $I_{\text{obs}}(v, J - v', J')$ is the observed line flux from the transition from level (v, J) to (v', J') , $A_{ul}(v, J - v', J')$ is the Einstein A radiative transition probability from level (v, J) to (v', J') , and $A(\lambda)$ is the extinction at the wavelength of that transition. As previously stated, the column densities calculated in this way assume a beam filling fraction of 1 for the H_2 emission; if the emission is clumpy, the column densities would then be a lower limit on the true value.

3.1. Extinction Correction

We find that the 0–0 S(3) line is anomalously weak, lying below the other 0–0 S lines in a Boltzmann plot (Figure 6), a

result that can be attributed to extinction from the 9.7 μm silicate feature (e.g., Lutz et al. 1996; Rodríguez-Fernández et al. 2001). In order to correct the observed H_2 lines for the extinction at mid-infrared wavelengths, we adopt the Fritz et al. (2011) extinction law derived from the *ISO* continuum toward Sgr A*. As extinction is a complicated function of the wavelength, we describe this law by taking the values of 100 data points on their derived curve from 0.43 to 25 μm and interpolating to obtain the extinction values at the observed wavelengths. The extinction values from Fritz et al. (2011) are then scaled in order to minimize the scatter in a linear fit to the S(1), S(2), S(3), and S(4) lines. We note that there is a significant improvement over the Lutz et al. (1996) law adopted by Rodríguez-Fernández et al. (2001). As can be seen in Figure 6, interpolating a fit using the same method is unable to bring the S(3) line into alignment with the S(2) and S(4) lines without assuming a much larger extinction, as well as overcorrecting the S(2) line to be brighter than the S(1). We note, however, that the extinction correction does not significantly change the measured temperatures.

The applied extinction correction using the Fritz et al. (2011) law significantly raises the flux of the S(3) line, making it consistent with the flux observed in the other 0–0 S pure

Table 2
Fitted Line Parameters for Northeast Region

λ	E_{upper}	g_J	Flux	Central ^a Velocity	Velocity ^b FWHM	Integrated Flux ^c	$N(\text{H}_2)^c$	A_λ	
(μm)	(K)		(Jy)	(km s^{-1})	(km s^{-1})	(Jy km s^{-1})	(cm^{-2})		
0–0 S(0)	28.221	510	5	<36.5	<3884	<1.3 × 10 ²¹	1.16
0–0 S(1)	17.035	1015	21	18.8 ± 0.4	7 ± 3	131 ± 3	2620 ± 111	5.29 ± 0.22 × 10 ¹⁹	1.88
0–0 S(2)	12.279	1682	9	18.9 ± 0.9	25 ± 5	101 ± 5	2034 ± 176	7.09 ± 0.62 × 10 ¹⁸	1.56
0–0 S(3)	9.665	2504	33	1.2 ± 0.2	13 ± 18	82 ± 18	106 ± 35	1.04 ± 0.35 × 10 ¹⁷	6.28
0–0 S(4)	8.026	3474	13	19.3 ± 0.2	46 ± 1	153 ± 1	3150 ± 49	1.15 ± 0.02 × 10 ¹⁸	1.20
0–0 S(5)	6.909	4586	45	40.6 ± 0.2	70 ± 0	178 ± 0	7720 ± 61	1.26 ± 0.01 × 10 ¹⁸	1.05
0–0 S(6)	6.109	5829	17	6.7 ± 0.2	44 ± 6	181 ± 6	1288 ± 74	1.09 ± 0.06 × 10 ¹⁷	1.27
0–0 S(7)	5.511	7197	57	15.8 ± 0.2	-3 ± 4	229 ± 4	3867 ± 110	1.86 ± 0.05 × 10 ¹⁷	1.11
0–0 S(8)	5.053	8677	21	5.1 ± 0.2	86 ± 6	134 ± 6	731 ± 54	2.17 ± 0.16 × 10 ¹⁶	1.16
0–0 S(9)	4.695	10263	69	7.2 ± 0.2	69 ± 4	126 ± 4	963 ± 54	1.89 ± 0.11 × 10 ¹⁶	1.51
0–0 S(10)	4.410	11940	25	1.1 ± 0.2	32 ± 24	112 ± 24	134 ± 44	1.84 ± 0.61 × 10 ¹⁵	1.25
0–0 S(11)	4.181	13703	81	2.6 ± 0.2	66 ± 12	136 ± 12	377 ± 56	3.76 ± 0.56 × 10 ¹⁵	1.33
0–0 S(12)	3.995	15549	29	0.5 ± 0.1	167 ± 66	191 ± 66	94 ± 54	7.18 ± 4.13 × 10 ¹⁴	1.35
0–0 S(13)	3.846	17458	93	0.9 ± 0.1	8 ± 34	175 ± 34	161 ± 51	9.56 ± 3.08 × 10 ¹⁴	1.42
0–0 S(14)	3.724	19402	33	<1.5	<155	<7.5 × 10 ¹⁴	1.52
0–0 S(15)	3.625	21400	105	<1.5	<156	<6.2 × 10 ¹⁴	1.62
1–0 Q(1)	2.407	6149	9	1.0 ± 0.0	87 ± 4	94 ± 4	95 ± 6	2.14 ± 2.14 × 10 ¹⁵	2.63
1–0 Q(2)	2.413	6471	5	<0.3	<43	<1.4 × 10 ¹⁵	2.62
1–0 Q(3)	2.424	6956	21	0.8 ± 0.0	77 ± 4	112 ± 4	94 ± 6	3.27 ± 3.27 × 10 ¹⁵	2.60
1–0 Q(4)	2.438	7584	9	0.3 ± 0.0	32 ± 9	83 ± 9	24 ± 4	8.75 ± 8.75 × 10 ¹⁴	2.57
1–0 Q(5)	2.455	8365	33	0.8 ± 0.0	66 ± 3	136 ± 3	113 ± 5	4.28 ± 4.28 × 10 ¹⁵	2.54
1–0 Q(6)	2.476	9286	13	0.3 ± 0.0	86 ± 7	74 ± 7	22 ± 3	8.80 ± 8.80 × 10 ¹⁴	2.50
1–0 Q(7)	2.500	10341	45	0.5 ± 0.0	100 ± 6	122 ± 6	67 ± 5	2.75 ± 2.75 × 10 ¹⁵	2.45
1–0 O(2)	2.627	5987	1	<0	<47	<5.4 × 10 ¹⁴	2.20
1–0 O(3)	2.803	6149	9	0.9 ± 0.0	71 ± 3	123 ± 3	120 ± 5	2.75 ± 0.13 × 10 ¹⁵	2.26
1–0 O(4)	3.004	6471	5	0.2 ± 0.0	76 ± 11	99 ± 11	23 ± 3	7.70 ± 1.32 × 10 ¹⁴	2.72
1–0 O(5)	3.235	6956	21	0.7 ± 0.0	68 ± 3	111 ± 3	86 ± 4	4.00 ± 0.19 × 10 ¹⁵	2.21
1–0 O(6)	3.501	7584	9	<0	<48	<3.1 × 10 ¹⁵	1.89
1–0 O(7)	3.808	8365	33	0.7 ± 0.2	18 ± 42	151 ± 42	105 ± 47	9.53 ± 4.29 × 10 ¹⁵	1.44
1–0 O(8)	4.162	9286	13	<2	<320	<4.2 × 10 ¹⁶	1.29

Notes.

^a Uncertainty in the wavelength calibration of *ISO* observations ranges from 25 to 60 km s^{-1} (Valentijn et al. 1996).

^b The spectral resolution of SWS observations ranges from 100 to 300 km s^{-1} (Valentijn et al. 1996).

^c Values are not corrected for extinction.

rotational lines. It indicates that the extinction in N and S is only slightly larger than that derived by Fritz et al. (2011) toward Sgr A* (note that as the extinction law is determined using the same *ISO* observations of Sgr A* that are analyzed here, we adopt the unscaled Fritz et al. (2011) extinction values for the latter source). However, minimizing the scatter in a linear fit to the first four detected rotational lines of H₂ does not account for the slight curvature seen in the Boltzmann plots of the H₂ lines. This method thus actually slightly overestimates the extinction, yielding a slightly overlarge flux for the S(3) line. We thus find that it is better to perform a simultaneous optimization of the fit to extinction and temperature, as described in the following section.

3.2. Discrete Temperature Fitting

We next plot the column densities $N(v, J)$ divided by the level degeneracy g_J against the upper-level energy $E(v, J)/k$ in a “Boltzmann plot.” For H₂ the level degeneracy is $g_J = g_s(2J + 1)$, where $g_s = 3$ for ortho-H₂ (odd J) and $g_s = 1$ for para-H₂ (even J). With the exception of the pointing toward Sgr A* (for which only five pure rotational lines are detected), the pure rotational lines measured toward

the CNB follow a convex or “positive” curve that is generally interpreted as the presence of multiple temperature components. While Neufeld (2012) has found that a sufficiently low density ($\log n < 4.8$) isothermal gas can also reproduce a positive curvature in a Boltzmann plot for CO pure rotational line emission, no work has yet searched for a similar effect with the H₂ molecule. Lacking this detailed modeling, we note that there are several reasons to suspect that this specialized case is not applicable to our H₂ measurements. First, the curvature induced in this way is slight and is not sufficient to explain many of the observations examined by Neufeld (2012) without still appealing to multiple temperature components. Second, lower critical densities of the pure rotational H₂ lines (Le Boulrot et al. 1999) suggest that substantially lower densities would be required, should this effect manifest in H₂ observations, while in fact the bulk of the CNB gas has higher densities: recent measurements of the density of CNB gas are in the range of $\log n = 4.5\text{--}6.5$ (Requena-Torres et al. 2012; Mills et al. 2013). We thus assume for this work that the substantial curvature in the Boltzmann plots indicates that the CNB gas is not isothermal.

Table 3
Fitted Line Parameters for Sgr A*

λ	E_{upper}	g_J	Flux	Central ^a Velocity (km s ⁻¹)	Velocity ^b FWHM (km s ⁻¹)	Integrated Flux ^c (Jy km s ⁻¹)	$N(\text{H}_2)^c$ (cm ⁻²)	A_V	
(μm)	(K)		(Jy)						
0–0 S(0)	28.221	510	5	<124.9	...	<13290	<4.3 × 10 ²¹	0.99	
0–0 S(1)	17.035	1015	21	<11.9	...	<1265	<2.6 × 10 ¹⁹	1.61	
0–0 S(2)	12.279	1682	9	<68.3	...	<7273	<2.5 × 10 ¹⁹	1.33	
0–0 S(3)	9.665	2504	33	<6.6	...	<698	<6.8 × 10 ¹⁷	5.37	
0–0 S(4)	8.026	3474	13	9.6 ± 1.3	2 ± 29	186 ± 29	6.96 ± 1.81 × 10 ¹⁷	1.02	
0–0 S(5)	6.909	4586	45	30.6 ± 1.8	36 ± 12	189 ± 12	6175 ± 662	1.01 ± 0.11 × 10 ¹⁸	0.90
0–0 S(6)	6.109	5829	17	7.1 ± 1.7	0 ± 40	147 ± 40	1110 ± 460	9.37 ± 3.89 × 10 ¹⁶	1.09
0–0 S(7)	5.511	7197	57	12.0 ± 1.2	53 ± 29	264 ± 29	3385 ± 629	1.63 ± 0.30 × 10 ¹⁷	0.95
0–0 S(8)	5.053	8677	21	4.7 ± 1.0	4 ± 25	105 ± 25	531 ± 198	1.58 ± 0.59 × 10 ¹⁶	1.00
0–0 S(9)	4.695	10263	69	<8.2	...	<871	<1.7 × 10 ¹⁶	1.29	
0–0 S(10)	4.410	11940	25	<8.0	...	<847	<1.2 × 10 ¹⁶	1.07	
0–0 S(11)	4.181	13703	81	<9.6	...	<1021	<1.0 × 10 ¹⁶	1.13	
0–0 S(12)	3.995	15549	29	<10.9	...	<1157	<8.8 × 10 ¹⁵	1.15	
0–0 S(13)	3.846	17458	93	<10.9	...	<1157	<6.9 × 10 ¹⁵	1.21	
0–0 S(14)	3.724	19402	33	<10.9	...	<1156	<5.6 × 10 ¹⁵	1.30	
0–0 S(15)	3.625	21400	105	<10.9	...	<1156	<4.6 × 10 ¹⁵	1.39	
1–0 Q(1)	2.407	6149	9	<0.7	...	<108	<2.4 × 10 ¹⁵	2.25	
1–0 Q(2)	2.413	6471	5	<0.6	...	<94	<3.0 × 10 ¹⁵	2.24	
1–0 Q(3)	2.424	6956	21	<0.5	...	<79	<2.8 × 10 ¹⁵	2.22	
1–0 Q(4)	2.438	7584	9	<0.4	...	<68	<2.5 × 10 ¹⁵	2.20	
1–0 Q(5)	2.455	8365	33	<0.4	...	<60	<2.3 × 10 ¹⁵	2.17	
1–0 Q(6)	2.476	9286	13	<0.3	...	<54	<2.1 × 10 ¹⁵	2.14	
1–0 Q(7)	2.500	10341	45	<0.4	...	<58	<2.4 × 10 ¹⁵	2.10	
1–0 O(2)	2.627	5987	1	<0	...	<60	<6.9 × 10 ¹⁴	1.88	
1–0 O(3)	2.803	6149	9	<0	...	<48	<1.1 × 10 ¹⁵	1.93	
1–0 O(4)	3.004	6471	5	<0	...	<37	<1.2 × 10 ¹⁵	2.33	
1–0 O(5)	3.235	6956	21	0.3 ± 0.1	34 ± 22	82 ± 22	24 ± 10	1.13 ± 0.47 × 10 ¹⁵	1.89
1–0 O(6)	3.501	7584	9	0.3 ± 0.1	66 ± 36	114 ± 36	39 ± 25	2.54 ± 1.62 × 10 ¹⁵	1.61
1–0 O(7)	3.808	8365	33	<11	...	<1735	<1.6 × 10 ¹⁷	1.23	
1–0 O(8)	4.162	9286	13	<10	...	<1563	<2.0 × 10 ¹⁷	1.10	

Notes.

^a Uncertainty in the wavelength calibration of *ISO* observations ranges from 25 to 60 km s⁻¹ (Valentijn et al. 1996).

^b The spectral resolution of SWS observations ranges from 100 to 300 km s⁻¹ (Valentijn et al. 1996).

^c Values are not corrected for extinction.

In order to constrain multiple temperatures present in the CND gas, we first follow the approach of Rosenthal et al. (2000) and perform a simultaneous fit to three temperature components in the pure rotational lines observed in the southwest and northeast regions (note that with the smaller number of lines detected toward Sgr A*, we can only justify fitting a single-temperature component in this source). The measured column densities are fit to a summation of three column densities from three single-temperature components (each of which would be a straight line in the Boltzmann plot):

$$N(v, J)/g_J = \sum_{i=1}^3 C_i e^{-E(v, J)/kT_{\text{ex}, i}}. \quad (2)$$

As before, $E(v, J)$ is the energy of level (v, J) , g_J is the level degeneracy, and $N(v, J)$ is the column density determined using Equation (1). The C_i are constants determined by our fitting, representing the contribution of each of the three components to the total column density, and the $T_{\text{ex}, i}$ are the temperatures of each component. We perform a minimization of the residuals of a least-squares fit to simultaneously determine the best-fit temperature (the inverse of the slope of the line) for each of the three temperature components, as well

as its contribution to the total column density (the y-intercepts or C_i for each component). In addition to letting the $T_{\text{ex}, i}$ and C_i for each component be free parameters in our fitting, we also allow the extinction value (used to calculate $N(v, J)$ from the observed line fluxes) to be a free parameter, in order to determine a more accurate extinction correction, given the curvature in the Boltzmann plot.

The results of this minimization are shown in Figure 8, and the best-fit $T_{\text{ex}, i}$, C_i , and $N_{\text{H}_2, i}$ for each component are given in Table 4. The extinction and the two lowest-temperature components (the “hot” and “hotter” gas) are well constrained by our data. The best-fit extinction is $0.98\times$ the extinction toward Sgr A* (or $A_{L'} = 1.07$) for the southwest region, and slightly higher for the northeast region: $1.17\times$ the extinction toward Sgr A* (or $A_{L'} = 1.28$). However, the highest-temperature or “hottest” component is not strongly constrained and is effectively a lower limit on the highest temperatures present ($\gtrsim 2600$ K, which is also approximately the temperature of the detected rovibrational Q(1) and O(1) lines of H₂ at these positions). However, we will use the best-fit values for the very hot component in our estimates of the total column density that follow. We find best-fit temperatures of 580, 1350, and 3630 K toward the southwest region and 520, 1260, and 2840 K toward

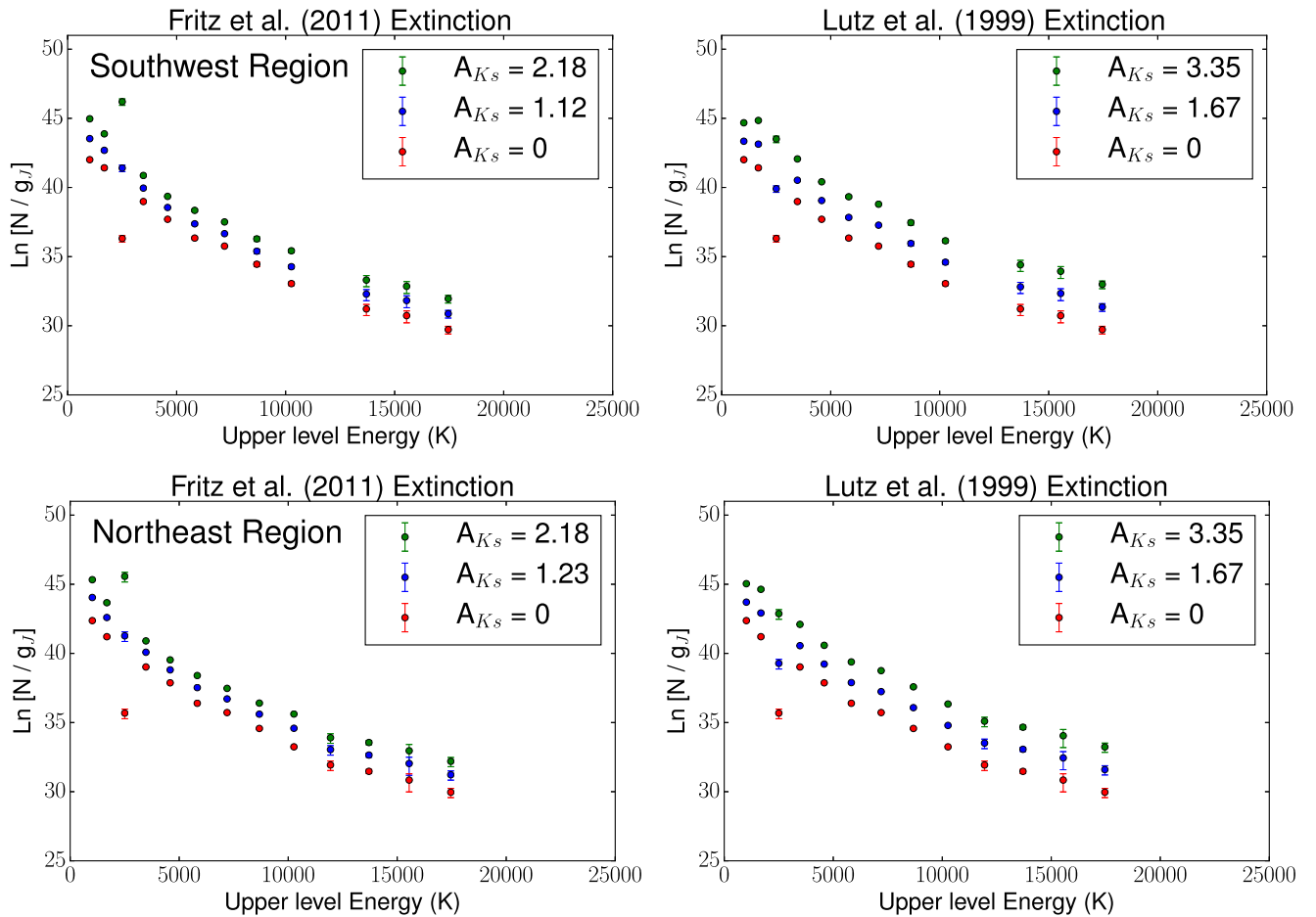


Figure 6. Boltzmann plots of the 0–0 S lines toward the southwest region and northeast region of the CN. Left: applying the extinction law derived by Fritz et al. (2011) from the *ISO* observations of Sgr A*. We show the column densities first uncorrected for extinction (red), then with an optimal correction fit in conjunction with the temperature components to minimize the residual scatter (blue), and finally for an overcorrection of the extinction (green). Right: applying the extinction law derived by Lutz et al. (1996) from the *ISO* observations of Sgr A*. We show the column densities first uncorrected for extinction (red), then with a correction equivalent to 30 mag of visual extinction (blue), and finally for the extinction correction needed to make the S(3) line consistent with neighboring lines (green).

Table 4
Fraction of Hot H₂

$T_{\text{ex},i}$ (K)	C_i^a (cm ⁻²)	$N_{\text{H}_2,i}$ (cm ⁻²)	Fraction of Hot H ₂
Southwest Region			
580	4.20×10^{19}	6.02×10^{20}	93.68%
1350	1.19×10^{18}	4.03×10^{19}	6.27%
3630	2.92×10^{15}	3.24×10^{17}	0.05%
Northeast Region			
520	8.82×10^{19}	1.13×10^{21}	94.14%
1260	2.21×10^{18}	6.93×10^{19}	5.76%
2840	1.56×10^{16}	1.24×10^{18}	0.10%

Note.

^a See Equation (2).

the northeast region. Toward Sgr A*, we separately fit a single-temperature component and find the best-fit temperature to be 1100 K. We find that the temperatures in the northeast region are 100–200 K cooler than in the southwest region. One possible explanation is that this is because the southwest region is closer to a source of heat provided by the central nuclear cluster. After all, only the southwest edge of the CN appears

to be ionized, while the northeast edge does not (Zhao et al. 1993). We discuss other alternatives in Section 4.2.2.

The extremes of temperature that we find are higher than temperatures that have been measured in the CN with other tracers. The hottest measured dust temperatures are 220 K (Cotera et al. 1999), and measurements of highly excited CO using *Herschel* by Goicoechea et al. (2013) find temperatures of ~ 1300 K toward the central cavity (consistent with our detection of $T = 1100$ K in this direction, though our detection of a single-temperature component in this region may be an observational bias, due to weaker lines and more variable spectral baselines in this region). The only measurements of comparably hot gas are of $T \sim 1700$ – 2500 K gas measured by Ciurlo et al. (2016) for other near-infrared rovibrational lines of H₂ in the inner edge and central cavity of the CN. However, there is a large uncertainty on the highest temperature they measure ($T \sim 2500_{-900}^{+3000}$), and the majority of the positions they analyze show significant deviations from a thermal distribution that they attribute to recent formation of H₂ in the central cavity. In contrast, we find that the 0–0 S lines in the northeast and southwest regions of the CN appear to be consistent with a thermal distribution up to temperatures of at least 2600 K.

The resulting Boltzmann diagrams of the extinction-corrected column density for each position are shown in

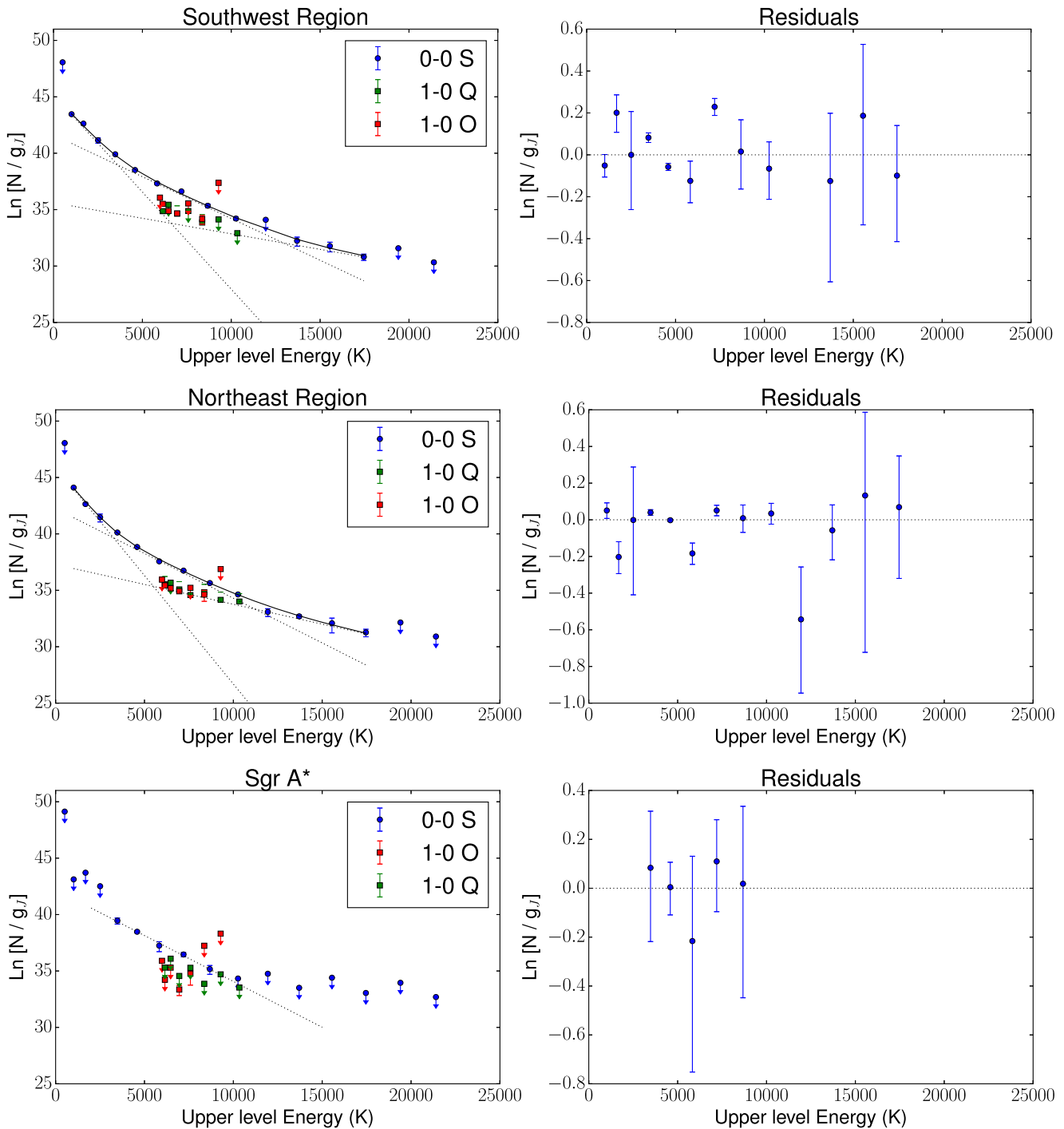


Figure 7. Boltzmann plots of the observed H₂ lines (0–0 S, 1–0 Q, and 1–0 O) toward the southwest region, northeast region, and Sgr A*. The plotted column densities have been calculated from line fluxes that have been corrected for extinction. Fits to the 0–0 S column densities for three discrete temperature components (dashed lines) and their summation (solid line) are shown for the southwest and northeast regions. The properties of these temperature components are given in Table 4. Only one temperature component (dashed line) can be fit toward Sgr A*. The residuals of the fits to the 0–0 S lines are also show in the left panels.

Figure 7. Each individual temperature component is plotted in the Boltzmann diagram as a dashed line, with the sum of all three components plotted as a solid line. In addition to the 0–0 S lines that are used in the temperature fit, we also plot the $\nu = 1 - 0$ O and Q rovibrational lines. We find that they follow a roughly straight line on these plots, lying below the pure rotational lines with similar upper-level energies. The temperature of these lines is roughly consistent with that of the highest-temperature gas component measured in the 0–0 S

lines (~ 3000 K). These two distinct distributions are in contrast to what is observed in the Orion KL outflow, in which the rotational and vibrational lines are thermalized and follow a single distribution in the Boltzmann diagram (Rosenthal et al. 2000; however, the high- J CO lines observed in Orion KL do show a curved distribution similar to the 0–0 S H₂ lines in the CND; e.g., Goicoechea et al. 2015). Although we do not detect the S(0) ($J = 2-0$) line, we can also estimate a T_{32} temperature from our measured upper limit on the strength of this line and

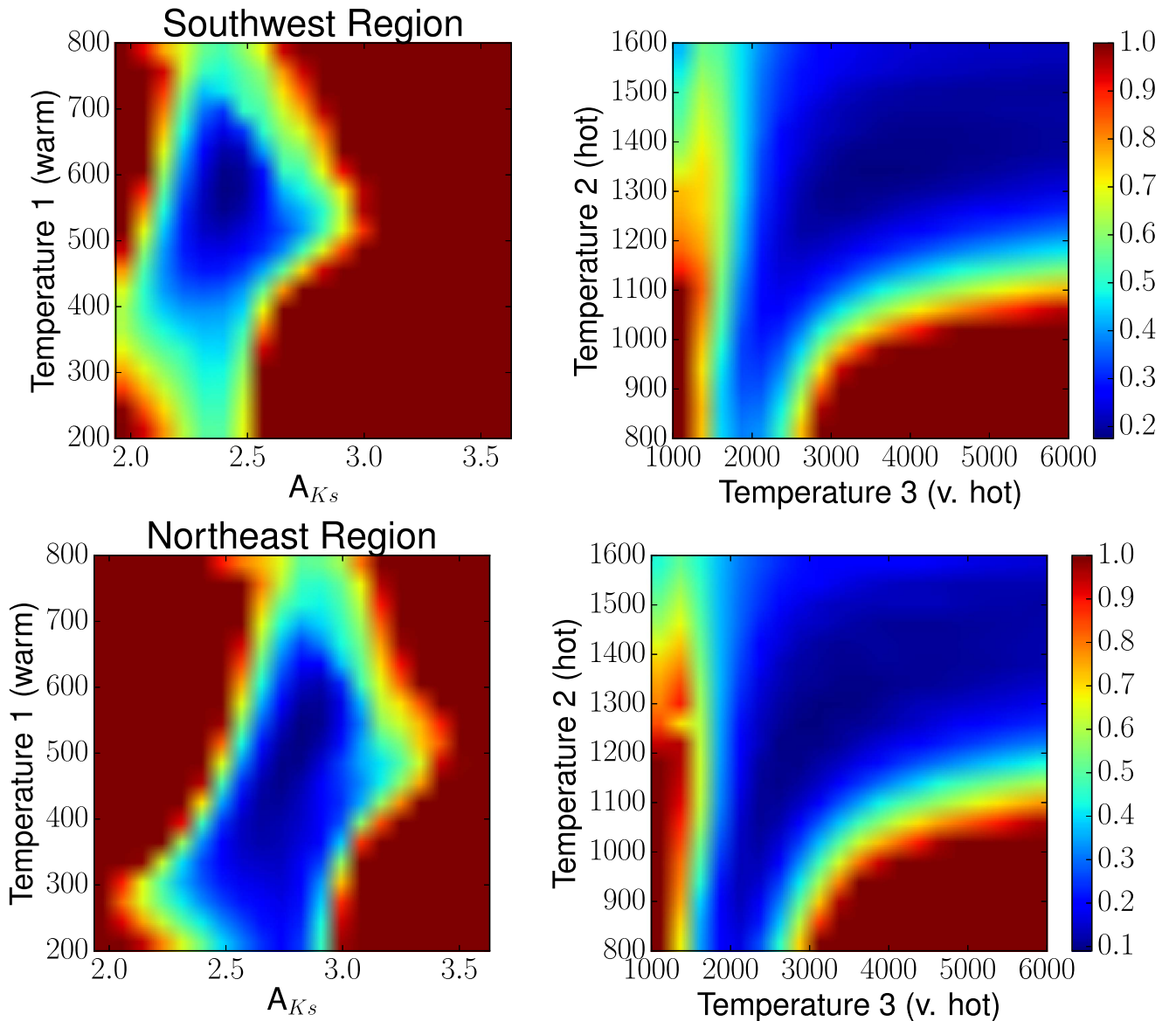


Figure 8. Plots of the residual scatter from simultaneous fits to the L' band ($\lambda = 3.776 \mu\text{m}$) extinction and three temperature components, showing the constraints that can be achieved for these four parameters. The color scale in these plots represents the reduced χ -squared value of the fit. In general, the L' -band extinction, warm temperature, and hot temperature are well constrained by these observations in both the southwest and northeast regions. However, the very hot temperature is less well constrained and is best understood as a lower limit on this value.

our measurement of the $S(1)$ ($J = 3-1$) line. We constrain $T_{32} > 110$ K in the southwest region and > 130 K in the northeast region.

Using the temperature fits, we can extrapolate the contribution of each component to lower J and determine the total column density of each temperature component. The fraction of the H_2 column in each component (“hot”/“hotter”/“hottest”) is given in Table 4. We find that for the northeast and southwest regions the vast majority of the detected H_2 is in the “hot” 500–600 K component: more than 95% for both sources. Both sources have 3%–4% of the H_2 column in the “hotter” 1200–1300 K component and less than 0.1% of the H_2 column in the “hottest” $T \sim 3000$ K component. While this makes both sources appear quite similar, the best-fit temperature components in the northeast region are somewhat cooler than those in the southwest region.

Summing over all the components, we can also estimate the total column of hot ($T > 500$ K) H_2 in each source. For the

southwest region we measure a total column of $6.4 \times 10^{20} \text{ cm}^{-2}$. For the northeast region we measure a total column of $1.2 \times 10^{21} \text{ cm}^{-2}$. As the fitting uncertainties are small, the dominant error in these quantities is likely the absolute flux calibration of ISO/SWS , which is estimated to be 12%–20% for the wavelength range studied here (Schaeidt et al. 1996). We thus find that there is significantly more hot H_2 in the northeast region (around a factor of 2) than in the southern region. This is consistent with our observations that the H_2 lines are stronger in the northeast than in the southwest.

3.3. Continuous Temperature Fitting

As we do not detect the $S(0)$ line in the ISO data, our discrete temperature fits are not very sensitive to the presence of “warm” gas with $T < 500$ K. Further, as the discrete fitting approach seeks to optimize a fit to three temperature components that are not consistent between the northeast and southwest regions, it is difficult to objectively compare the hot

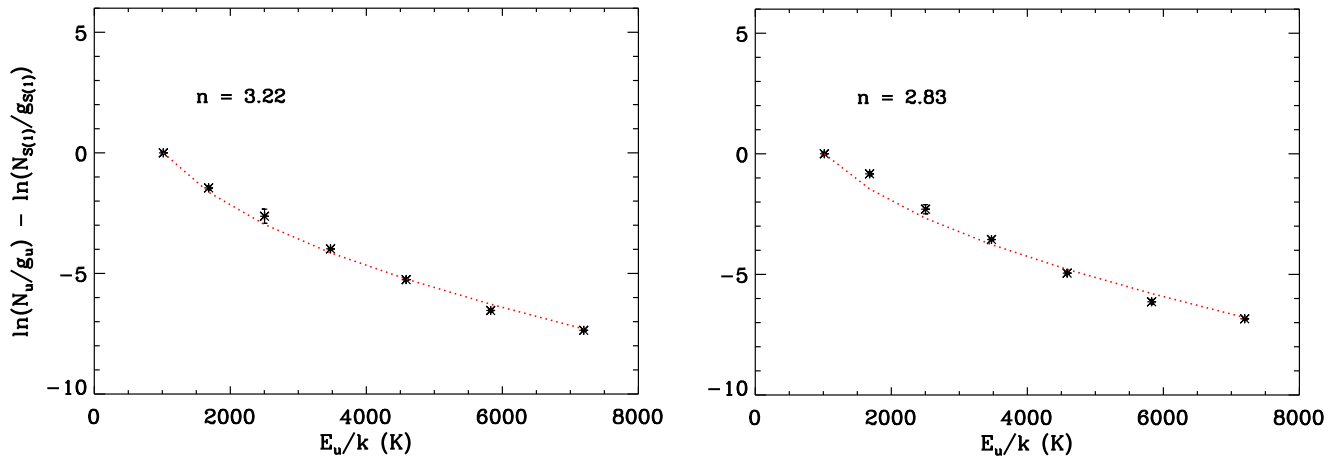


Figure 9. Fits to the observed 0–0 S(1) through 0–0 S(7) H₂ lines for a power-law distribution of temperatures toward the northeast (left) and southwest (right) regions. The plotted column densities have been calculated from line fluxes that have been corrected for extinction.

gas properties (such as the fraction of gas at each temperature) between these two sources. We thus also employ a second approach for quantifying the temperature differences between the northeast and southwest regions.

Here, we first assume that a fixed number of discrete temperature components is not a physically well-motivated model for this gas, and that a more realistic description would be gas in which the temperature varies smoothly or continuously from cool to hot values, as can be generated by a range of pre-shock densities, shock velocities, or shock geometries (Neufeld & Yuan 2008; Yuan & Neufeld 2011; Appleton et al. 2017). We then follow the approach of Togi & Smith (2016) by adopting a continuous power-law temperature distribution for the H₂, which extrapolates the temperature distribution down to lower values than those we were able to measure. In this model, the measured column densities of H₂ molecules are modeled as the distribution from a power-law function with respect to temperature, $dN \propto T^{-n} dT$, where dN is the number of molecules in the temperature range $T \rightarrow T + dT$. The model then consists of just three adjustable parameters: an upper- and lower-temperature cutoff (T_u and T_l) and a power-law index (n).

As our primary goals in adopting this model are to compare the power-law indices between the two observed regions and to make an estimate of the total amount of H₂ that could be present if this power law extends to lower temperatures ($T < 500$ K), we focus only on the S(1)–S(7) lines. We also keep the upper temperature, T_u , fixed at 2000 K, as hotter gas is a negligible contributor to the total column. The only two parameters that then vary in the model fitting are the lower cutoff temperature T_l and the power-law index n . We then use this model to fit the observed column densities for the northeast and southwest lobes (corrected for the best-fit extinction value that was determined in our discrete temperature fits). We report results for two adopted values of a lower cutoff temperature: $T = 50$ K, roughly consistent with the coolest molecular gas typically measured in other clouds in the Galactic center (Ao et al. 2013; Ginsburg et al. 2016), and $T = 100$ K, which is roughly the coolest gas allowed by our nondetection of the S(0) line (though given the large upper-level energy of this line, cooler gas may be present that would not contribute emission to this line).

Figure 9 shows the resulting model fits to the observed H₂ columns for the southwest and northeast regions. We find that a

fit to a continuous temperature distribution shows that the southwest region ($n = 2.83$) is systematically warmer than the northeast region ($n = 3.22$), where a shallower or smaller power-law index indicates a greater fraction of warm/hot gas. This is consistent with the trend seen in our discrete temperature fits that the northeast region appears systematically cooler than the southwest region. The power-law indices measured for both regions of the CND are much shallower than typical values measured in the centers of other star-forming galaxies, indicating that the CND gas is hotter than typical gas in the nuclei of other galaxies (Togi & Smith 2016). We will discuss this further in Section 4.1.

The best-fit power law for each region can then be extended to lower temperatures in order to estimate the total column of warm H₂ with temperatures greater than the assumed cutoff value (50 or 100 K). Adopting a cutoff value of 100 K for the coolest gas present, we measure a total column of warm H₂ of $1.2 \times 10^{22} \text{ cm}^{-2}$ for the northeast region and $4.4 \times 10^{21} \text{ cm}^{-2}$ for the southwest region. In this case, there is ~ 3.5 times more warm ($T > 100$ K) H₂ present in the northeast region than in the southwest region, compared to twice as much hot ($T > 500$ K) H₂ in the northeast, as measured from the discrete temperature fits. The warm H₂ column would also be ~ 4 – 5 times larger than the hot column that we measured with our discrete temperature fits. If we go further and adopt a lower cutoff temperature of 50 K, the total column of H₂ present would be $5.6 \times 10^{22} \text{ cm}^{-2}$ for the northeast region and $1.6 \times 10^{22} \text{ cm}^{-2}$ for the southwest region. This is again ~ 3.5 times more warm ($T > 100$ K) H₂ present in the northeast region than in the southwest region. The overall increase in H₂ column would also mean that if this power-law extrapolation holds, and if there is gas as cool as 50 K in the CND, 70%–80% of the H₂ would have temperatures in the range of 50–100 K. We discuss this further in Section 4.4.

3.4. The Warm/Hot Gas Mass of the CND and the Central Cavity

We can also translate these total column densities of H₂ into total masses within the observed ISO/SWS aperture for the extrapolated amount of warm ($T > 50$ or 100 K) gas and the measured amount of hot ($T > 500$ K) gas. The total H₂ mass M_{H_2} is given by

$$M_{\text{H}_2} = N_{\text{H}_2} \Omega d^2 \mu_{\text{H}_2} m_{\text{H}}, \quad (3)$$

Table 5
CND Masses

Tracer	Aperture (arcsec \times arcsec)	Total Molecular Mass ^a	
		(M_{\odot})	
		Southwest Region	Northeast Region
H ₂ (discrete temperature fit, $T > 500$ K)	14 \times 20	6.1	11.4
H ₂ (power-law extrapolation, $T > 100$ K)	14 \times 20	41	111
H ₂ (power-law extrapolation, $T > 50$ K)	14 \times 20	146	518
Dust continuum (C. Battersby et al. 2017, in preparation)	14 \times 20	456	370
CO (Requena-Torres et al. 2012)	22	557 ^b	413 ^b

Notes.

^a Masses given are the total molecular mass, assuming a mean molecular weight of 2.8, consistent with the Galactic center metallicity.

^b Scaled to an area equivalent to a 14'' \times 20'' aperture, assuming a uniform flux distribution.

where N_{H_2} is the total measured column density of H₂; Ω is the solid angle of the *ISO*/SWS aperture; d is the distance to the Galactic center (8 kpc; Boehle et al. 2016); μ_{H_2} is the mean molecular weight of the gas, which we take to be 2.8, assuming abundances of 71% H, 27% He, and 2% metals (e.g., Kauffmann et al. 2008); and m_{H} is the mass of a hydrogen atom. Taking an aperture size of 14'' \times 20'' (0.54 by 0.78 pc on the sky, at the assumed distance of 8 kpc), the measured total column densities from our discrete temperature fits would correspond to a total mass of hot molecular gas of 6.1 M_{\odot} in the southwest region and 11.4 M_{\odot} in the northeast region.

Additionally, we can determine the mass of hot molecular gas in the central cavity from the observation toward Sgr A* (for just the measured 1100 K temperature component). Here we find a total mass of $\sim 0.5 M_{\odot}$ within the *ISO*/SWS aperture. In comparison, there is measured to be roughly 30 M_{\odot} of ionized gas in the minispiral and 300 M_{\odot} of neutral gas in the central cavity (Jackson et al. 1993). This is a larger mass of hot H₂ in the central cavity than measured by Ciurlo et al. (2016), who estimate a total H₂ mass of $\sim 7 \times 10^{-3} M_{\odot}$ if the emission they observe is representative of emission along a narrow inner edge of the CND that abuts the central cavity. However, unlike the high-resolution observations of Ciurlo et al. (2016), and as we discuss in Section 4.3, it is not clear that all of the gas we detect toward Sgr A* is actually confined to the central cavity. There is then no requirement that this hot gas be associated (solely) with the inner edge of the CND or the central cavity.

The total molecular mass of gas inferred to be present from our extrapolated continuous temperature fits is much larger than the mass of just the hot gas determined from the discrete temperature fits. For a cutoff temperature of 100 K, the total molecular gas mass in the southwest region would be 41 M_{\odot} , and for the northeast region it would be 111 M_{\odot} . For a lower cutoff temperature of 50 K, the total molecular gas mass in the southwest region would be $146 \pm 54 M_{\odot}$, and for the northeast region it would be $518 \pm 243 M_{\odot}$.

We can compare these masses to other independent estimates of the total molecular gas mass in these regions. CO observations by Requena-Torres et al. (2012) inferred masses of 795 M_{\odot} and 590 M_{\odot} toward nearly identical positions in the southwest and northeast, respectively, for a beam with FWHM = 22''.5. As these are just masses of H₂ (R. Torres 2017, private communication), we first scale these masses for the adopted mean molecular weight. As the solid angle of this beam is approximately twice the *ISO* aperture, we also scale the masses to the *ISO* aperture, assuming uniform emission. The

resulting masses for the southwest (557 M_{\odot}) and northeast (413 M_{\odot}) regions are also reported in Table 5. We can also measure a molecular mass from the H₂ columns determined from *Herschel* dust measurements (C. Battersby et al. 2017, in preparation; C. Battersby et al. 2017, private communication). These H₂ column densities were derived by fitting a modified blackbody to each pointing in the Galactic center, with the dust temperature allowed to vary as a free parameter. The dust opacity as a function of frequency is determined by fitting a power law to tabulated opacities from Ossenkopf & Henning (1994) and assuming a constant gas-to-dust ratio of 100 and dust with a β of 1.75 over the entire Galactic center, yielding a frequency-dependent dust opacity of $\kappa_{\nu} = \kappa_0(\nu/\nu_0)^{\beta}$, where κ_0 is 4.0 cm² g⁻¹ at 505 GHz (the method is described in more detail in Battersby et al. 2011). Toward the southwest region, we measure an H₂ column of 4.9×10^{22} cm⁻² in the *ISO* aperture, and toward the northeast region, we measure an H₂ column of 4.0×10^{22} cm⁻², both consistent with the values shown in the column density maps of Etxaluze et al. (2011). These column densities correspond to total molecular gas masses of 456 M_{\odot} in the southwest region and 370 M_{\odot} in the northeast region.

If our power-law extrapolation is valid, and if 50 K is the correct cutoff temperature for the CND, then the total molecular mass we infer from this method for the northeast (southwest) region would account for 140% (32%) of the total molecular mass inferred from the dust emission, or 125% (26%) of the total molecular mass inferred from the CO observations. In contrast, the column of hot ($T > 500$ K) H₂ measured from our discrete temperature fits toward the northeast (southwest) region only accounts for 6% (2%) of the total H₂ column inferred from the dust emission and 5% (2%) of the total molecular mass inferred from the CO observations.

We find that dust and CO yield relatively consistent estimates of the total molecular gas within the *ISO* aperture; however, the molecular gas masses extrapolated from our continuous temperature fits to H₂ deviate significantly. In the southwest region, our mass estimate from H₂ is only one-quarter to one-third of the total molecular gas measured from CO and dust. In contrast, in the northeast region, the mass estimate from H₂ is significantly larger than the total molecular gas measured from CO and dust. This extreme variation is largely due to the fact that the southwest region has fainter H₂ and a correspondingly lower column density than the northeast region but is significantly brighter in CO and dust (and thus has a higher inferred total column of H₂). The discrepancy we find

suggests that extrapolations of a power-law temperature fit being used to estimate total molecular gas masses in extragalactic sources should be treated with caution, without a good understanding of where the extrapolation may become invalid. We further discuss several potential sources of this discrepancy in Section 4.4.

4. Discussion

4.1. The CNB Compared to Other Sources

To understand how the temperature of the warm H_2 and the fraction of gas at these temperatures in the CNB match up with the properties of other sources, we first compare the CNB to observations of other Galactic center molecular clouds. The pure rotational 0–0 S(0), S(1), S(3), S(4), and S(5) lines of H_2 were observed in a sample of 16 clouds in the central 500 pc of the Galaxy by Rodríguez-Fernández et al. (2001). As they used the Lutz et al. (1996) law to correct for the extinction of their sample, we have taken their reported line fluxes and redone the extinction correction using the Fritz et al. (2011) law in order to be more consistent with our CNB analysis. We select a subset of five clouds from their sample, all of which have detections of the 0–0 S(4) and S(5) lines. Fitting a power-law temperature distribution to these clouds as we did for the CNB, we find power-law indices that range from 4.7 to 5.0, with fits shown in Figure 10. These are steeper than the power-law indices we measure in the northeast ($n = 3.22$) and southwest ($n = 2.83$) regions of the CNB and indicate that the H_2 in typical Galactic center clouds is cooler than in the CNB. This is consistent with a comparison of the mean T_{76} for the five of these clouds for which the S(5) line could be detected (700 K; Rodríguez-Fernández et al. 2001) with what we would measure for T_{76} from our CNB data: 800 K for the southwest region and 870 K for the northeast region.

Similar to what we find when comparing to other molecular clouds in the central 500 pc of our Galaxy, the power-law index for the temperature distribution in the southwest and northeast regions of CNB (about 3) is also flatter than for any galaxies in the sample measured by Togi & Smith (2016), which includes galaxies with star-forming nuclei, luminous and ultraluminous infrared galaxies (LIRGS and ULIRGS), low-ionization nuclear emission-line regions (LINERs), Seyfert galaxies, dwarf galaxies, and radio galaxies. Measured power-law indices for this sample ranged from 3.79 to 6.4, with an average value of ~ 4.84 . The star-forming galaxies selected from the SINGS sample (Kennicutt et al. 2003) had a slightly lower average power-law index of 4.5, but they still do not approach the low values that we measure in the CNB. Even in the extreme shocked regions of Stephan’s Quintet, the power-law index is only measured to be ~ 4.2 (Appleton et al. 2017).

A direct comparison of these values is complicated because of the different scales involved: the CNB comprises only a few parsecs in the center of our Galaxy, while many of the measurements from Togi & Smith (2016) average over entire galaxies. Of course, the H_2 -emitting region of a galaxy may be much more compact: in the sample of ULIRGS, the mid-infrared H_2 emission is typically concentrated in the central 1 kpc to a few kiloparsecs (Higdon et al. 2006). Differences therefore could be either because, even in galaxies more extreme than the Milky Way, conditions similar to the CNB of our Galaxy are not present over larger (hundreds of parsec) scales, or because such conditions are present but are diluted by

abundant H_2 in less extreme conditions at larger radii. In support of the latter scenario, we note that the “typical” power-law indices we measure for clouds in the central 500 pc of our Galaxy (a region known to have higher temperatures, density, and turbulence than the disk of our Galaxy) appear quite comparable to those on kiloparsec scales in the centers of more extreme star-forming and infrared-bright galaxies.

4.2. The Heating Mechanism for the CNB

4.2.1. The Excitation Mechanism of H_2 in the CNB

For highly excited lines of H_2 like those we analyze here, there are two possibilities for their excitation: collisional excitation, in which the observed levels are populated by collisions with other H_2 molecules, atoms, or electrons in energetic shocks (e.g., Shull & Beckwith 1982), and fluorescent excitation, in which the observed levels are populated by decay into lower states after the resonant absorption of ultraviolet photons in the Lyman and Werner bands (e.g., Gould & Harwit 1963; Black & Dalgarno 1976). Collisional excitation can be thought of as a “bottom-up” population of the levels of H_2 , as persistent collisions in shocks with temperatures of thousands of kelvin thermally excite H_2 out of its ground state and into the observed rotationally and vibrationally excited states. In contrast, fluorescent excitation can be thought of as a “top-down” population of the levels of H_2 , as the molecules are directly excited into high vibrational levels by the resonant absorption of ultraviolet wavelength photons, and a fraction of the molecules, instead of dissociating, de-excite into the observed lower-excitation rotation and vibration states. A number of observational diagnostics exist to distinguish between these two excitation mechanisms, which focus on the relative brightness of rotational and highly vibrationally excited transitions (the latter of which are expected to be weaker or absent in the case of shock-excited emission; Shull & Hollenbach 1978; Black & van Dishoeck 1987; Wolfire & Konigl 1991).

Although fluorescent emission might seem to be ruled out owing to the large radii at which the “very hot” H_2 traced by the 1–0 Q(1) line is observed, UV radiation from the central star cluster is not the only possible source of this excitation: cosmic rays, as they impact the dense gas, can also excite the Lyman and Werner bands of H_2 (Prasad & Tarafdar 1983). Due to the limited sensitivity and wavelength range of the SWS spectra, we lack detections of many of these traditional tracers of fluorescent emission (e.g., more highly vibrationally excited lines like the 1–0 S(1) line at $2.1217 \mu\text{m}$ and the 2–1 S(1) line at $2.2476 \mu\text{m}$; Shull & Hollenbach 1978). However, Tanaka et al. (1989) previously observed these diagnostic lines toward both the southwest and northeast lobes of the CNB, using the UKIRT telescope. They find that these sources, referred to as Sgr A SW and NE, respectively, both have line ratios consistent with purely thermal excitation. Similarly, Ciarlo et al. (2016) measure the 1–0 S(1)/2–1 S(1) in the central cavity of the CNB (the central $36'' \times 29''$) and find regions where the excitation is dominated by both fluorescent and collisional excitation. However, in the region that is likely most similar to the CNB gas probed by the *ISO* observations (their “Zone 1” on the inner edge of the CNB, with a far stronger 1–0 S(1) line flux than in other locations analyzed), they find that the line ratios are consistent with collisional heating alone. We

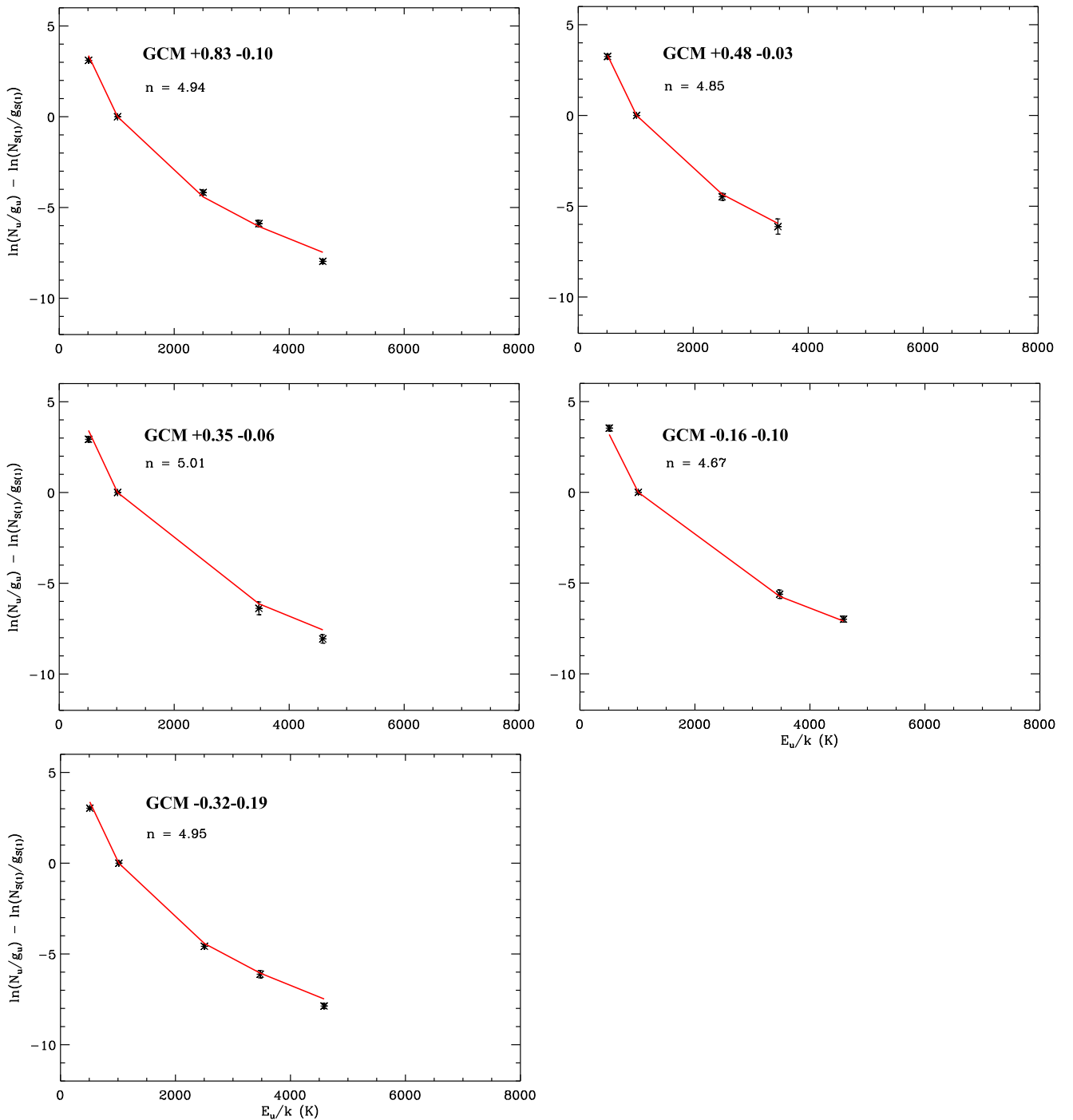


Figure 10. Boltzmann plots of the observed H₂ lines (0–0 S) toward five Galactic center clouds from the observations of Rodríguez-Fernández et al. (2001). The plotted column densities have been calculated from line fluxes that have been corrected for extinction and scaled to the observed aperture size for each line. Fits to the 0–0 S column densities for a power-law distribution of temperatures are shown.

thus conclude that the H₂ lines we observe toward the northeast and southwest regions of the CNB are collisionally excited.

We also search for anomalous ortho-to-para ratios in our observed H₂ lines. The typical signature of disequilibrium in the ortho-to-para ratio is a zigzag or sawtooth pattern in the Boltzmann diagram, where the ortho (odd J) lines appear systematically weaker than lines from the para (even J) transitions. We do see a slight sawtooth pattern in the S(1)–S(5) lines from the southwest region; however, the magnitude of the variation in these lines is consistent with the random scatter

seen in the higher pure rotational lines. We find no evidence for an anomalous ortho-to-para ratio in the observed pure rotational lines of H₂ for the other two positions: this characteristic pattern does not appear in the residuals of the temperature fits for the northeast region or toward Sgr A*. Anomalous ratios have previously been seen in the pure rotational 0–0 S lines of several Galactic center clouds (Rodríguez-Fernández et al. 2000), as well as in the 1–0 S lines observed by Ciurlo et al. (2016) in several positions in the central cavity of the CNB. Such ratios have been attributed to

the recent formation and/or destruction of H_2 before it can reach ortho-to-para equilibrium via, e.g., proton-exchange collisions with H^+ , H_3^+ , or H_3O^+ (Gerlich 1990; Le Bourlot et al. 1999).

4.2.2. Shock Heating and Line Cooling

Based on the continuous distribution of warm to very hot temperatures we measure with the pure rotational lines of H_2 and the line ratios measured by Ciurlo et al. (2016), we favor a scenario in which the warm/hot H_2 in the CNB is heated in shocks. The presence of gas at temperatures in excess of 2000 K likely rules out dissociative shocks as the primary source of this heating, as the H_2 molecules must survive to the post-shock phase in order to reach these temperatures, as opposed to dissociating and reforming at cooler temperatures (~ 500 K; Hollenbach & McKee 1989).

Although either shocks or a high cosmic-ray ionization rate are favored by chemical modeling of millimeter and submillimeter molecular lines in the CNB (Harada et al. 2015), heating by cosmic rays appears unlikely to be sufficient to produce the observed fractions of gas at these high temperatures (Clark et al. 2013). This is consistent with the observed *Herschel* far-infrared line ratios measured by Goicoechea et al. (2013) toward the central cavity, which are also suggested to rule out both cosmic rays and X-rays for heating the hot ($T \sim 1300$ K) gas. Photon-dominated regions (PDRs) as the sole source of heating in the CNB were initially ruled out by Bradford et al. (2005), based on the observed ratio of CO 7–6 and [O I] 63 μm lines compared to predictions from PDR models (e.g., Kaufman et al. 1999). However, this conclusion was based on the assumption that a clumpy PDR model with high-density gas like that applied to the Orion Bar (e.g., Burton et al. 1990) is not applicable to the CNB, when in fact more recent analyses have found that there is gas with significantly higher densities ($n \sim 2 \times 10^5$ – 3×10^6 cm^{-3} ; Requena-Torres et al. 2012; Mills et al. 2013) than the Bradford et al. (2005) measurement ($n \sim (5$ – $6) \times 10^4$ cm^{-3}). The presence of higher-density clumps could allow for a more sizable contribution from PDR heating; however, given that the CO 7–6/[O I] 63 μm ratio in the CNB is still an order of magnitude below a clumpy classical PDR like the Orion Bar (Stacey et al. 1993), and that apparently very hot gas is also located at large separations from the central star cluster, it is still not likely that this is the sole source of heating in the CNB. Some PDR heating could be supported by our measurement that the southwest region (the edge of which is ionized) is warmer than the northeast region. However, higher spatial resolution observations of the H_2 emission in conjunction with an improved 3D model of the molecular gas in the CNB are needed to determine whether this difference is consistent with a radial trend in heating that would be expected for a PDR driven by the central star cluster.

While the post-shock line emission resulting from a single planar C-shock model is well approximated as arising from an isothermal temperature distribution (e.g., Kaufman & Neufeld 1996; Neufeld et al. 2006), C-shocks (even single C-shocks) can also match power-law temperature distributions like those we observe. For example, single C-type bow shock models yield a temperature distribution with a power-law index β of 3.8 (e.g., Neufeld & Yuan 2008). Different values of β can originate from different properties of single shocks (e.g., a bow shock with a less curved structure should yield lower β ; Yuan

& Neufeld 2011) or multiple shocks (e.g., a mix of shock geometries, or a range of pre-shock densities, or a mix of shock velocities in which some shocks are sufficiently energetic to dissociate H_2 ; Neufeld & Yuan 2008; Yuan & Neufeld 2011; Appleton et al. 2017). Single bow shock models are traditionally applied to stellar jets and outflows and are likely less applicable to the complex geometry of CNB gas. However, a range of shock velocities (given the large turbulent line widths) and a range of pre-shock densities (e.g., multiple density components are measured by Requena-Torres et al. 2012) are both plausible scenarios for the CNB.

C-shocks as the dominant mode of heating the CNB would be consistent with Rodríguez-Fernández et al. (2004), who find that PDRs can only contribute 10%–30% of the heating for gas in Galactic center clouds outside of the CNB. They favor moderate-velocity shocks ($v \sim 25$ km s^{-1}) induced by turbulent motions as the primary heating source in these clouds, for example, contributing to the warm H_2 measured by Rodríguez-Fernández et al. (2001) toward a number of these sources. For the CNB, chemical modeling by Harada et al. (2015) favors shocks with $v > 40$ km s^{-1} for reproducing the observed abundances of species in millimeter and submillimeter observations. However, such velocities are near those required to dissociate H_2 molecules, and so velocities $\gtrsim 40$ km s^{-1} are likely ruled out by our observations of H_2 at temperatures > 2600 K, which are also consistent with what is found for the peak temperatures in C-shock models with $v \sim 25$ – 30 km s^{-1} . Shock velocities > 25 km s^{-1} and correspondingly higher temperatures in the CNB would be consistent with recent work that suggests that turbulent heating is responsible for a correlation between temperature and line width in Galactic center molecular clouds (Immer et al. 2016), as the CNB has much broader line widths than other Galactic center clouds ($\sigma \sim 10$ – 40 km s^{-1} on 0.2 pc scales; Montero-Castaño et al. 2009), compared to predicted and observed $\sigma \sim 0.5$ – 5 km s^{-1} for other Galactic center clouds (Shetty et al. 2012; Kauffmann et al. 2013; Rathborne et al. 2015). In order to explain the higher temperatures measured in the southwest, we would predict that careful analysis of the northeast and southwest regions would find larger line widths in the southwest and more signatures of shocks.

In addition to providing insight into the gas heating mechanisms, the observed H_2 lines also make an important contribution to cooling the CNB gas. Summing together the extinction-corrected fluxes of all of the observed pure rotational lines of H_2 , and again using our adopted distance of 8 kpc, we measure a total H_2 luminosity of $275 L_\odot$ toward the northeast region, $200 L_\odot$ toward the southwest region, and $100 L_\odot$ toward Sgr A* and the central cavity. The CNB luminosities can be compared to CO luminosities from Bradford et al. (2005), who conduct large velocity gradient (LVG) modeling based on CO observations and estimate a CO luminosity-to-mass ratio of $1.4 L_\odot/M_\odot$ for the entire CNB. If we apply this to the CO masses adapted from Requena-Torres et al. (2012) in Table 5, this would equate to total CO luminosities of roughly $580 L_\odot$ toward the northeast region and $780 L_\odot$ toward the southwest region. The H_2 lines would then contribute roughly 50% and 25% of the cooling generated by the CO line in the northeast and southwest regions, respectively. For the CO conditions modeled by Bradford et al. (2005) (a uniform temperature of 240 K), the authors predicted that the H_2 luminosity would be 30% of CO luminosity, which is similar to

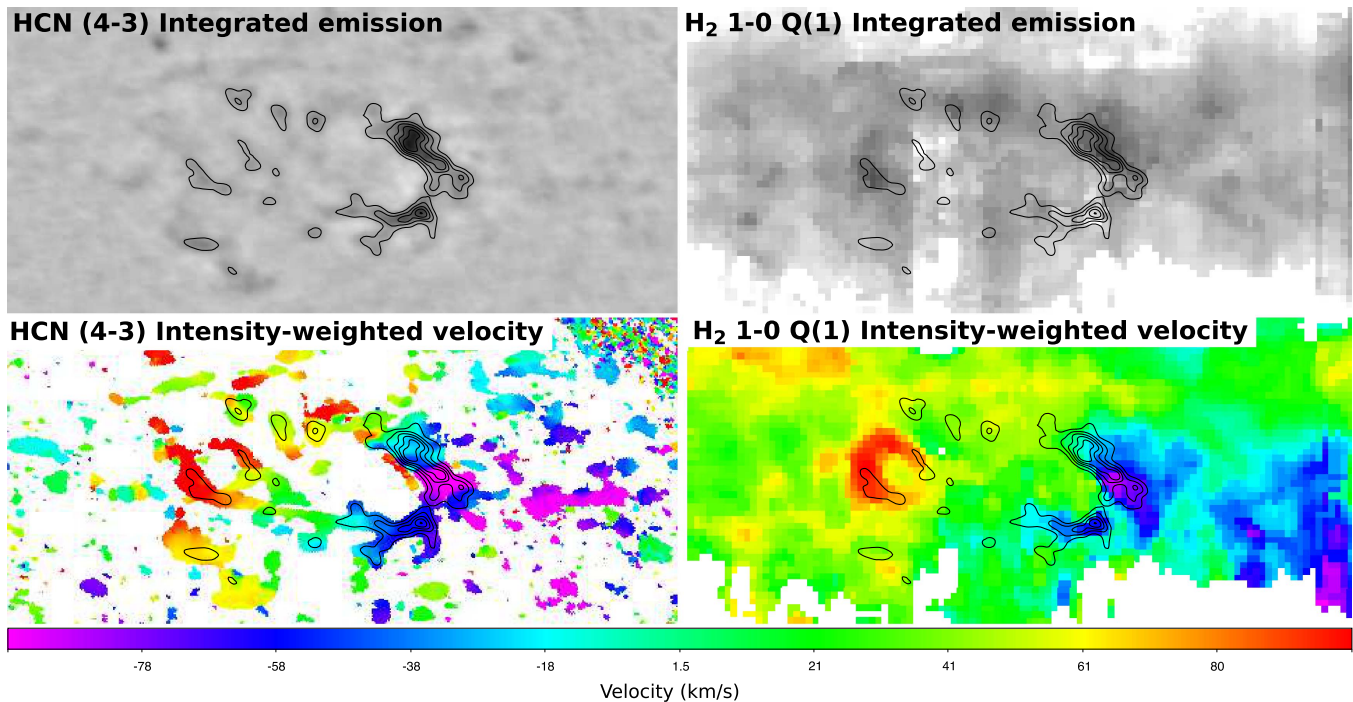


Figure 11. Comparison of emission from HCN $J = 4 - 3$ (left; Montero-Castaño et al. 2009) and H₂ 1–0 Q(1) transitions (right; Feldmeier et al. 2014) toward the CND, oriented to be in Galactic coordinates. Top row: integrated emission (moment 0) map. Bottom row: intensity-weighted velocity (moment 1). Contours are the HCN $J = 4 - 3$ integrated emission.

the contribution we measure, though apparently originating in hotter gas. In the central cavity, however, H₂ appears to provide a more significant fraction of the molecular gas cooling. Using observations of the far-infrared CO lines, Goicoechea et al. (2013) measure $L_{\text{CO}} = 125 L_{\odot}$ toward the central $30'' \times 30''$. This is roughly three times the area of the aperture of the *ISO* observations, for which we measure $L_{\text{H}_2} = 100 L_{\odot}$ toward the central cavity, indicating that H₂ is likely the dominant cooling line for molecular gas interior to the CND. However, this is still only a small fraction of the cooling from the atomic gas in the central cavity through far-infrared fine-structure lines (e.g., $L_{[\text{O III}]}$ = 885 L_{\odot} , $L_{[\text{O I}]}$ = 885 L_{\odot} , and $L_{[\text{C II}]}$ = 230 L_{\odot} in a $30'' \times 30''$ aperture; Goicoechea et al. 2013).

4.3. The Spatial Distribution of the Warm Gas

Given that the *ISO* spectra analyzed here consist of three large-aperture pointings toward the central parsecs and thus have extremely limited spatial information, one question is where the measured H₂ is actually located. Prior observations (e.g., Etxaluze et al. 2011; Goicoechea et al. 2013; Lau et al. 2013; Ciurlo et al. 2016) have pointed to the central cavity and the inner edge of the CND as the location of both the hottest gas and dust. However, the resolution of our *ISO* data is not sufficient to distinguish between these locations, nor are the kinematics sufficiently precise to be indicative of a particular location (though the average velocities of the *ISO* northwest and southwest region spectra are broadly consistent with the kinematics of dense gas in the CND; e.g., Christopher et al. 2005). However, the high-resolution maps of the 1–0 Q(1) line published in Feldmeier et al. (2014) and reproduced here in Figure 1 can give some insight into the distribution of the hottest H₂ in the central parsecs. We can clearly see peaks in the flux of the 1–0 Q(1) line at the positions of our *ISO* apertures centered on the northeast and southwest regions.

Importantly, even in this highly excited H₂ line (which, as noted above, is consistent with being thermalized at $T < 2600$ K), these peaks in the highest column density of the very hot H₂ are nearly cospatial with the peaks of cooler molecular gas and dust, as can be seen in a comparison with a map of HCN 4–3 from Montero-Castaño et al. (2009) in Figure 11. In fact, emission from the 1–0 Q(1) line is clearly not confined just to the central cavity or a narrow inner edge of the CND, but is present at radii from 1 to 5 pc from Sgr A* and the central nuclear cluster. Further, as can be seen in Figure 11, it is not simply the spatial distributions of H₂ and HCN that appear similar, but the gas kinematics as well. Hence, although prior observations of hot molecular gas and dust in the central parsecs have suggested that this gas is primarily found in the central cavity and minispiral (Cotera et al. 1999; Goicoechea et al. 2013; Ciurlo et al. 2016) and the inner edge of the CND (Lau et al. 2013; Ciurlo et al. 2016), the observations of Feldmeier et al. (2014) suggest that it is more broadly distributed throughout the CND. This is important for understanding what is heating the gas, and we return to this point in Section 4.2.

As expected, the column of hot H₂ is not greatest toward Sgr A* (in the central cavity, which is believed to be largely evacuated, containing only a few tens of solar masses of ionized gas and a few hundred solar masses of neutral gas; Jackson et al. 1993). It is also not clear in these *ISO* observations whether we are even detecting central cavity gas in the pointing toward Sgr A*. Due to large noise and poor baseline shapes for this position, we only detect enough lines of H₂ to constrain a single ~ 1110 K temperature component. The velocity of the H₂ lines toward this position (28 ± 25 km s^{−1}) could be consistent with the velocity of gas in the nearby 50 and 20 km s^{−1} clouds, which recent orbital models place $\gtrsim 50$ pc in the foreground of Sgr A* (Kruijssen et al. 2015). The

spectra also do not clearly have a broader line width than the other positions, which would be expected if this were indeed gas closer to Sgr A*, with higher orbital speeds consistent with those seen in the ionized minispiral (Zhao et al. 1993). Hence, although Ciurlo et al. (2016) appear to detect gas in the central cavity in their higher-resolution maps of near-infrared rovibrational lines, we cannot clearly say that the gas we detect toward Sgr A* is any closer to the central black hole than the CNB gas detected in other positions.

Despite the lack of detailed spatial information in the *ISO* data, we do notice several key differences between the H₂ emission toward the northeast and southwest regions of the CNB. First, the H₂ lines are stronger for a given *J* in the northeast region than in the southwest region. Not surprisingly, the total column of warm H₂ in the northeast region is twice as large as in the southwest region. However, even though the lines are brighter in the northeast region, the extinction toward the northeast region is slightly larger. Interestingly, this is the reverse of what is typically observed in the emission from other molecular species, where the northeast region generally appears much weaker than the southwest region (Requena-Torres et al. 2012; Mills et al. 2013).

4.4. Interpreting the Mass of Warm H₂ in the CNB

Using the measured power-law temperature distributions to measure a total H₂ column by extrapolating to a common cutoff temperature of 50 K, we find that relative to estimates based on dust continuum emission and CO line emission we overestimate the molecular gas mass in the northeast region and underestimate the mass in the southwest region. This indicates that determining masses in this way is not straightforward, and may even not be valid for certain scenarios. In order to begin to assess the factors that determine whether the extrapolation of a power-law temperature distribution yields a valid H₂ mass in the CNB, we focus on several key assumptions of this analysis. The first is that $T = 50$ K (or $T = 100$ K) is a valid cutoff temperature for the gas in the CNB. A second major assumption is that the extrapolation of the power-law index derived using the S(1) lines and above is valid for the lower temperatures of interest here. A third assumption is that we are able to detect all of the emitting H₂ in our aperture (there are no local extinction effects). Finally, in order to put the measured quantities in context, we must assume that either CO or dust is a reliable indicator of the total H₂ column.

4.4.1. The Cutoff Temperature

We first address the assumption that a temperature of 50 or 100 K is a valid cutoff temperature for the distribution of gas temperatures in the CNB. First, in order to match the mass estimates from CO and the dust continuum, the cutoff temperature should be above 50 K in the northeast region and below 50 K in the southwest region. Immediately, this appears inconsistent with the general trend seen that the southwest region is warmer than the northeast. However, we also want to examine whether there is any additional evidence that such cold gas could exist in this region. The coolest rotational temperature we can directly measure through our discrete temperature fits is 580 K in the southwest region and 520 K in the northeast region. The nondetection of the S(0) line suggests that there may be an additional gas component with temperature >110 K (>130 K). However, this is not so strongly constraining as to rule out separate and yet cooler

temperature components, including gas too cool to significantly excite the S(0) line. The best constraint on this cold material comes from the dust, as temperatures as low as 25 K have been measured for the CNB (Etxaluz et al. 2011). Although dust and gas temperatures are not globally observed to be in thermal equilibrium in the Galactic center, dust temperatures of 20–30 K are typically associated with gas temperatures of 50–70 K in other Galactic center clouds (Ginsburg et al. 2016), suggesting that the presence of gas significantly cooler than 50 K is unlikely.

A cutoff temperature of 50 K also implies that the bulk of the gas ($\sim 70\%$ – 80%) is cold ($T < 100$ K). Although gas temperatures of 50 K are not excluded by excitation analyses of HCN (Mills et al. 2013), the CO analysis of Requena-Torres et al. (2012) found that the temperature of the CO must be greater than 150 K (based on the observed ratio of ¹²CO and ¹³CO lines). While this would appear to rule out cutoff temperatures as low as 50 or even 100 K, we note that without any cool gas the total H₂ column we infer would be entirely inconsistent with the H₂ column inferred from these same CO observations. Either there is cooler gas present, or we are not detecting a large fraction of the H₂ emission from the CNB. We thus do not yet rule out the possibility of a cutoff temperature as low as 50 K for the CNB gas. However, this scenario then requires a significant burden of observational proof, including an explanation of the observed CO isotope ratios (either as an average on large scales that is not representative of the isotope ratios on smaller scales, or due to some type of anomaly), and verification of $T = 50$ or 100 K gas with direct measurements using other tracers (e.g., NH₃, CH₃CN, CH₃CCH).

4.4.2. The Extrapolation of a Single Power-law Temperature Fit

In order to infer a total gas mass by extrapolating our H₂ data to temperatures below those that are measured, the power-law temperature distribution we fit to the S(1) and higher lines must also be valid for the lower-temperature gas. In observations of the centers of normal spirals and star-forming galaxies that include the detection of the S(0) line, there is no evidence for a break in the power law between the S(0) and S(1) lines (Togi & Smith 2016). Further, extrapolating the power-law distribution of H₂ column densities to a temperature of 50 K in these galaxies appears to consistently recover the total H₂ column as inferred through measurements of CO. This would support the adoption of a single power-law distribution for describing the range of temperatures present in the CNB gas. Alternatively, if the gas in the CNB were not consistent with a single power-law description of the temperature, this could account for the small (and varying; 6%–140%) fraction of the total (CO and dust-derived) H₂ column that is recovered in the southwest and northeast regions of the CNB. However, a more complicated temperature profile would seem to require a unique physical mechanism in this region that does not operate on kiloparsec scales in the center of other galaxies. Although the local line widths and densities in CNB may be slightly more extreme than the average conditions over kiloparsec scales in the center of our own and other galaxies (e.g., Montero-Castaño et al. 2009; Mills et al. 2013), at present we do not have a good justification for invoking the additional complexity of a varying power-law index.

4.4.3. Local Variations in the Extinction

Another possible factor that could explain the fact that total H_2 column derived from our power-law extrapolation of the pure rotational lines and that derived from CO or dust are not completely consistent (especially in the southwest region) is clumpy extinction. In this scenario, the lower column of pure rotational line emission observed in the southwest region (where stronger emission from dense gas tracers is observed; Montero-Castaño et al. 2009) might be due to having more of the gas hidden by higher local extinction in the clumpy structures that carry the bulk of the mass. If extinction did hide some of the H_2 emission in the CND, this could relax the tension we found from comparison with the CO observations of Requena-Torres et al. (2012) that both require the H_2 to be hotter than 150 K and infer a larger total H_2 column than can be matched with our direct observations of H_2 even when extrapolating to 50 K. A cutoff temperature of 150 K would then not be inconsistent with a total column inferred directly from H_2 that is much less than that derived with CO (or dust).

We note that due to the flat shape of the extinction law from 2 to 20 μm (Fritz, and our plots of extinction), higher clumpy extinction for one region should not manifest as any change in temperature, as emission would be uniformly missing for all of the observed rotational lines. However, the fact that the extinction is actually measured to be slightly higher in the northeast region (while it would need to be higher in the southwest region to hide more of the H_2 emission) would seem to argue against the scenario we propose. Ultimately, higher spatial and spectral resolution observations are needed to directly compare the clumpy structure observed in other molecules with the structure of the H_2 emission and to compare the kinematic components directly traced by H_2 and other molecules to confirm that H_2 is not subject to significant local extinction and that the H_2 is indeed observed to be fully and proportionately intermixed with the gas traced by other molecules.

4.4.4. Proxies for the Total H_2 Mass

We find that the total molecular mass inferred from two proxies for H_2 , observations of multiple lines of ^{12}CO and ^{13}CO (Requena-Torres et al. 2012) and column density maps derived from *Herschel* dust emission (C. Battersby et al. 2017, in preparation; C. Battersby et al. 2017, private communication), is generally consistent. The dust-derived masses are slightly lower than the CO-derived masses: by a factor of 1.2 in the southwest and 1.1 in the northeast. However, the CO-derived mass has been scaled to the size of the *ISO* aperture (as the aperture for the CO observations is significantly larger) assuming that the emission is uniform across this aperture. If this emission is not uniform, then there could be a larger discrepancy between these masses. Given that the dust-derived mass is consistent with the CO-derived mass and that the Galactic center consists of relatively high metallicity gas, we also do not expect that CO-dark gas is a substantial component of the CND.

While it is possible that there could be additional systematic uncertainties in these mass determinations (e.g., in the adopted $[^{12}\text{CO}]/[H_2]$ abundance of 8×10^{-5} used by Requena-Torres et al. (2012) to determine the CO-to- H_2 conversion, or in the assumption for the dust of a given dust mass opacity κ , a constant gas-to-dust ratio of 100, or a β of 1.75 over the entire Galactic

center), the consistency of the masses inferred from both CO and dust suggests that these are unlikely to be significant.

4.4.5. The Total H_2 Mass

We can make an extremely rough estimate of the total molecular mass of the CND by using the maps of the Q(1) line flux from Feldmeier et al. (2014) to scale the masses determined from the rotational H_2 lines in the observed *ISO* apertures. The two $14'' \times 20''$ *ISO* apertures covering the northeast and southwest regions contain only $\sim 1/13$ of the total Q(1) emission seen by Feldmeier et al. (2014) over the central 9.5×8 pc of the CND. If the brightness distributions of the rotational lines we use to determine the mass and of the rovibrational Q(1) line of H_2 are similar, then we would infer that the total mass of gas with $T > 50$ K in the CND is $\sim 8600 M_\odot$. This is $\sim 15\%$ – 40% of the total molecular mass of gas ($(2\text{--}5) \times 10^4 M_\odot$) estimated to be present in the CND (Etzaluze et al. 2011; Requena-Torres et al. 2012). However, there are likely to be significant differences in the distributions of rotational and rovibrational lines, so this estimate should be treated with caution. We also note that the estimates of the total mass from CO and dust also suffer from limitations: the mass estimate from Requena-Torres et al. (2012) is extrapolated from LVG fits in just two apertures over a limited velocity range, and the estimate from Etzaluze et al. (2011), while covering the bulk of the CND, is limited to a central radius of 1.75 pc.

5. Conclusion

We have analyzed archival *ISO* observations of the spectra of three positions toward the central parsecs of our Galaxy, pointed toward the central supermassive black hole Sgr A* and the northeast and southwest regions of the CND. Below, we summarize the main findings of this paper:

1. In both the northwest and southeast regions of the CND we detect emission from pure rotational lines of H_2 up to the 0–0 S(13) lines, as well as from a handful of rovibrational transitions.
2. From the pure rotational lines of H_2 , we are able to fit three discrete temperature components to the hot gas toward both regions of the CND. We find slightly lower best-fit temperatures in the northeast region (520, 1260, and 2840 K) than in the southwest region (580, 1350, and 3630 K), although in both cases the highest temperature present is loosely constrained and is best interpreted as a lower limit of $T \gtrsim 2600$ K.
3. From our discrete temperature fits, we measure a total column and mass of hot H_2 that are approximately twice as large for the northeast region ($N_{H_2} = 1.20 \times 10^{21} \text{ cm}^{-2}$, $M_{H_2} = 11.4 M_\odot$) as for the southwest region ($N_{H_2} = 6.43 \times 10^{20} \text{ cm}^{-2}$, $M_{H_2} = 6.1 M_\odot$). Comparing these columns to the total column of H_2 estimated from CO and dust emission, we estimate that the warm/hot H_2 represents between 0.2% and 2% of all of the H_2 in the CND.
4. We also fit a continuous, power-law distribution of temperatures to the observed pure rotational lines of H_2 . We find a power-law index that is higher in the northeast (3.22) than in the southwest (2.83), confirming that the molecular gas is warmer in the southwest region of the CND. These power-law indices are also higher than those we measure for other clouds in the Galactic center (4.7–5.0) and higher than previously measured for other galaxies (3.79–6.4; Togi & Smith 2016).

5. Extrapolating the power-law distribution we fit down to a temperature of 50 K, we would estimate a total mass of $146 M_{\odot}$ for the southwest region and $518 M_{\odot}$ for the northeast region. For the southwest (northeast) region, these masses represent 32% (140%) of the total molecular mass inferred from measurements of the dust emission from C. Battersby et al. (2017, in preparation; C. Battersby et al. 2017, private communication) and 26% (125%) of the total molecular mass inferred from measurements of the CO emission (Requena-Torres et al. 2012).
6. Based on the observed H_2 properties, as well as prior work measuring the spatial distribution and line ratios of rovibrationally excited H_2 , we favor C-shocks as the primary excitation mechanism for the warm/hot H_2 and the dominant heating source for the CN D gas.

We especially thank the anonymous referee for their work in making extremely detailed and helpful comments that significantly improved the presentation of these results. E.A.C.M. thanks Nadine Neumayer for drawing attention to H_2 observations of the circumnuclear disk and Anya Feldmeier-Krause for sharing her 1–0 Q(1) data of the central 8 pc. A.T. is grateful for support from the National Science Foundation under grant no. 1616828.

ORCID iDs

Aditya Togi  <https://orcid.org/0000-0001-5042-3421>

Michael Kaufman  <https://orcid.org/0000-0002-2521-1985>

References

- Ao, Y., Henkel, C., Menten, K. M., et al. 2013, *A&A*, **550**, A135
- Appleton, P. N., Guillard, P., Togi, A., et al. 2017, *ApJ*, **836**, 76
- Baganoff, F. K., Maeda, Y., Morris, M., et al. 2003, *ApJ*, **591**, 891
- Battersby, C., Bally, J., Ginsburg, A., et al. 2011, *A&A*, **535**, A128
- Black, J. H., & Dalgarno, A. 1976, *ApJ*, **203**, 132
- Black, J. H., & van Dishoeck, E. F. 1987, *ApJ*, **322**, 412
- Boehle, A., Ghez, A. M., Schödel, R., et al. 2016, *ApJ*, **830**, 17
- Bradford, C. M., Stacey, G. J., Nikola, T., et al. 2005, *ApJ*, **623**, 866
- Burton, M. G., Hollenbach, D. J., & Tielens, A. G. G. M. 1990, *ApJ*, **365**, 620
- Christopher, M. H., Scoville, N. Z., Stolovy, S. R., & Yun, M. S. 2005, *ApJ*, **622**, 346
- Ciurlo, A., Paumard, T., Rouan, D., & Clénet, Y. 2016, *A&A*, **594**, A113
- Clark, P. C., Glover, S. C. O., Ragan, S. E., Shetty, R., & Klessen, R. S. 2013, *ApJL*, **768**, L34
- Cotera, A., Morris, M., Ghez, A. M., et al. 1999, in ASP Conf. Ser. 186, The Central Parsecs of the Galaxy, ed. H. Falcke et al. (San Francisco, CA: ASP), 240
- de Graauw, T., Haser, L. N., Beintema, D. A., et al. 1996, *A&A*, **315**, L49
- Ekers, R. D., van Gorkom, J. H., Schwarz, U. J., & Goss, W. M. 1983, *A&A*, **122**, 143
- Etaluzze, M., Smith, H. A., Tolls, V., Stark, A. A., & González-Alfonso, E. 2011, *AJ*, **142**, 134
- Feldmeier, A., Neumayer, N., Seth, A., et al. 2014, *A&A*, **570**, A2
- Fritz, T. K., Gillessen, S., Dodds-Eden, K., et al. 2011, *ApJ*, **737**, 73
- Genzel, R., Crawford, M. K., Townes, C. H., & Watson, D. M. 1985, *ApJ*, **297**, 766
- Gerlich, D. 1990, *JChPh*, **92**, 2377
- Ginsburg, A., Henkel, C., Ao, Y., et al. 2016, *A&A*, **586**, A50
- Godard, B., & Cernicharo, J. 2013, *A&A*, **550**, A8
- Goicoechea, J. R., Chavarría, L., Cernicharo, J., et al. 2015, *ApJ*, **799**, 102
- Goicoechea, J. R., Etaluzze, M., Cernicharo, J., et al. 2013, *ApJL*, **769**, L13
- Goto, M., Indriolo, N., Geballe, T. R., & Usuda, T. 2013, *JPCA*, **117**, 9919
- Goto, M., Usuda, T., Nagata, T., et al. 2008, *ApJ*, **688**, 306
- Gould, R. J., & Harwit, M. 1963, *ApJ*, **137**, 694
- Güsten, R., Genzel, R., Wright, M. C. H., et al. 1987, *ApJ*, **318**, 124
- Güsten, R., Walmsley, C. M., Ungerechts, H., & Churchwell, E. 1985, *A&A*, **142**, 381
- Harada, N., Riquelme, D., Viti, S., et al. 2015, *A&A*, **584**, A102
- Herrnstein, R. M., & Ho, P. T. P. 2002, *ApJ*, **579**, L83
- Higdon, S. J. U., Armus, L., Higdon, J. L., Soifer, B. T., & Spoon, H. W. W. 2006, *ApJ*, **648**, 323
- Hollenbach, D., & McKee, C. F. 1989, *ApJ*, **342**, 306
- Hüttemeister, S., Wilson, T. L., Bania, T. M., & Martín-Pintado, J. 1993, *A&A*, **280**, 255
- Immer, K., Kauffmann, J., Pillai, T., Ginsburg, A., & Menten, K. M. 2016, *A&A*, **595**, A94
- Indriolo, N., & McCall, B. J. 2012, *ApJ*, **745**, 91
- Jackson, J. M., Geis, N., Genzel, R., et al. 1993, *ApJ*, **402**, 173
- Kauffmann, J., Bertoldi, F., Bourke, T. L., Evans, N. J., II, & Lee, C. W. 2008, *A&A*, **487**, 993
- Kauffmann, J., Pillai, T., & Zhang, Q. 2013, *ApJL*, **765**, L35
- Kaufman, M. J., & Neufeld, D. A. 1996, *ApJ*, **456**, 611
- Kaufman, M. J., Wolfire, M. G., Hollenbach, D. J., & Luhman, M. L. 1999, *ApJ*, **527**, 795
- Kennicutt, R. C., Jr., Armus, L., Bendo, G., et al. 2003, *PASP*, **115**, 928
- Kessler, M. F., Steinz, J. A., Anderegg, M. E., et al. 1996, *A&A*, **315**, L27
- Kruijssen, J. M. D., Dale, J. E., & Longmore, S. N. 2015, *MNRAS*, **447**, 1059
- Lau, R. M., Herter, T. L., Morris, M. R., Becklin, E. E., & Adams, J. D. 2013, *ApJ*, **775**, 37
- Le Bourlot, J., Pineau des Forêts, G., & Flower, D. R. 1999, *MNRAS*, **305**, 802
- Lee, S., Pak, S., Choi, M., et al. 2008, *ApJ*, **674**, 247
- Lo, K. Y., & Claussen, M. J. 1983, *Natur*, **306**, 647
- Longmore, S. N., Bally, J., Testi, L., et al. 2013, *MNRAS*, **429**, 987
- Lu, J. R., Do, T., Ghez, A. M., et al. 2013, *ApJ*, **764**, 155
- Lugten, J. B., Stacey, G. J., Harris, A. I., Genzel, R., & Townes, C. H. 1987, in AIP Conf. Ser. 155, The Galactic Center, ed. D. C. Backer (Melville, NY: AIP), 118
- Lutz, D., Feuchtgruber, H., Genzel, R., et al. 1996, *A&A*, **315**, L269
- Lutz, D., Sturm, E., Genzel, R., et al. 2000, *ApJ*, **536**, 697
- Martin, C. L., Walsh, W. M., Xiao, K., et al. 2004, *ApJS*, **150**, 239
- Martín, S., Martín-Pintado, J., Montero-Castaño, M., Ho, P. T. P., & Blundell, R. 2012, *A&A*, **539**, A29
- Mills, E. A. C., Butterfield, N., Ludovici, D. A., et al. 2015, *ApJ*, **805**, 72
- Mills, E. A. C., Güsten, R., Requena-Torres, M. A., & Morris, M. R. 2013, *ApJ*, **779**, 47
- Mills, E. A. C., & Morris, M. R. 2013, *ApJ*, **772**, 105
- Montero-Castaño, M., Herrnstein, R. M., & Ho, P. T. P. 2009, *ApJ*, **695**, 1477
- Narayan, R., Mahadevan, R., Grindlay, J. E., Popham, R. G., & Gammie, C. 1998, *ApJ*, **492**, 554
- Neufeld, D. A. 2012, *ApJ*, **749**, 125
- Neufeld, D. A., Melnick, G. J., Sonnentrucker, P., et al. 2006, *ApJ*, **649**, 816
- Neufeld, D. A., & Yuan, Y. 2008, *ApJ*, **678**, 974
- Ossenkopf, V., & Henning, T. 1994, *A&A*, **291**, 943
- Prasad, S. S., & Tarafdar, S. P. 1983, *ApJ*, **267**, 603
- Rathborne, J. M., Longmore, S. N., Jackson, J. M., et al. 2015, *ApJ*, **802**, 125
- Requena-Torres, M. A., Güsten, R., Weiß, A., et al. 2012, *A&A*, **542**, L21
- Rodríguez-Fernández, N. J., Martín-Pintado, J., de Vicente, P., et al. 2000, *A&A*, **356**, 695
- Rodríguez-Fernández, N. J., Martín-Pintado, J., Fuente, A., et al. 2001, *A&A*, **365**, 174
- Rodríguez-Fernández, N. J., Martín-Pintado, J., Fuente, A., & Wilson, T. L. 2004, *A&A*, **427**, 217
- Rosenthal, D., Bertoldi, F., & Drapatz, S. 2000, *A&A*, **356**, 705
- Schaeidt, S. G., Morris, P. W., Salama, A., et al. 1996, *A&A*, **315**, L55
- Shetty, R., Beaumont, C. N., Burton, M. G., Kelly, B. C., & Klessen, R. S. 2012, *MNRAS*, **425**, 720
- Shull, J. M., & Beckwith, S. 1982, *ARA&A*, **20**, 163
- Shull, J. M., & Hollenbach, D. J. 1978, *ApJ*, **220**, 525
- Sloan, G. C., Kraemer, K. E., Price, S. D., & Shipman, R. F. 2003, *ApJS*, **147**, 379
- Smith, I. L., & Wardle, M. 2014, *MNRAS*, **437**, 3159
- Stacey, G. J., Jaffe, D. T., Geis, N., et al. 1993, *ApJ*, **404**, 219
- Tanaka, M., Hasegawa, T., Hayashi, S. S., Brand, P. W. J. L., & Gatley, I. 1989, *ApJ*, **336**, 207
- Togi, A., & Smith, J. D. T. 2016, *ApJ*, **830**, 18
- Valentijn, E. A., Feuchtgruber, H., Kester, D. J. M., et al. 1996, *A&A*, **315**, L60
- Wolfire, M. G., & Konigl, A. 1991, *ApJ*, **383**, 205
- Yuan, Y., & Neufeld, D. A. 2011, *ApJ*, **726**, 76
- Yusef-Zadeh, F., Cotton, W., Viti, S., Wardle, M., & Royster, M. 2013a, *ApJL*, **764**, L19
- Yusef-Zadeh, F., Royster, M., Wardle, M., et al. 2013b, *ApJL*, **767**, L32
- Yusef-Zadeh, F., Stolovy, S. R., Burton, M., Wardle, M., & Ashley, M. C. B. 2001, *ApJ*, **560**, 749
- Yusef-Zadeh, F., Wardle, M., Sewilo, M., et al. 2015, *ApJ*, **808**, 97
- Zhao, J.-H., Desai, K., Goss, W. M., & Yusef-Zadeh, F. 1993, *ApJ*, **418**, 235